

UNIVERSITY OF AMSTERDAM

MASTERS THESIS

Morphology analysis on micro-CT scans of saccular otoliths of the European hake

Supervisors:

Author:

Steven RAAIJMAKERS

dr. Robert Bellemans

dr. Jaap Kaandorp

Quinzia Palazzo MSc

*A thesis submitted in partial fulfilment of the requirements
for the degree of Master of Science in Computational Science*

in the

Computational Science Lab

Informatics Institute

December 2020



Declaration of Authorship

I, Steven RAAIJMAKERS, declare that this thesis, entitled ‘Morphology analysis on micro-CT scans of saccular otoliths of the European hake’ and the work presented in it are my own. I confirm that:

- This work was done wholly or mainly while in candidature for a research degree at the University of Amsterdam.
- Where any part of this thesis has previously been submitted for a degree or any other qualification at this University or any other institution, this has been clearly stated.
- Where I have consulted the published work of others, this is always clearly attributed.
- Where I have quoted from the work of others, the source is always given. With the exception of such quotations, this thesis is entirely my own work.
- I have acknowledged all main sources of help.
- Where the thesis is based on work done by myself jointly with others, I have made clear exactly what was done by others and what I have contributed myself.

Date: 1 August 2020

UNIVERSITY OF AMSTERDAM

Abstract

Faculty of Science
Informatics Institute

Master of Science in Computational Science

**Morphology analysis on micro-CT scans of saccular otoliths of the
European hake**

by Steven RAAIJMAKERS

The otoliths are three paired calciferous and proteinaceous structures found in the inner ear of teleost fish. They act as mechanoreceptors for hearing and equilibrium and their investigation can provide important information on the fish's biological history.

The proximal face of the saccular otolith, houses the sulcus acusticus, an important anatomical structure that is in contact with the sensory epithelium. The size of the sulcus acusticus relative to the size of the saccular otolith is assumed to alter the fish's hearing abilities. The effects of this ratio have not been researched extensively since it is difficult to reliably quantify the dimensions of the sulcus. In this thesis, we present a method to partition the sulcus from micro-CT scans of the saccular otoliths of European hake specimens of different sizes and sex. Subsequently, we perform experiments where we observed a linear relationship between the sulcus surface area and the otolith surface area (SSA : OSA ratio). The average SSA : OSA ratio for mature hakes is significantly lower in comparison to juveniles. Additionally, we found a linear relationship between the sulcus volume and the otolith volume (SV : OV ratio). In comparison to the SSA : OSA ratio, the SV : OV ratio is more evenly distributed between juvenile and mature hakes.

Thereafter, we examined the saccular otolith curvature, which is characterized by several protuberances. In this thesis, we present a method to detect the protuberances from the micro-CT scans of the saccular otoliths. We found the number of protuberances for juvenile hakes to increase with the fish length. Furthermore, we observed a sex dimorphism where female saccular otoliths contain higher numbers of protuberances than male saccular otoliths of equal fish length. Finally, we examined the curvature development of the saccular otolith through the derivation of its overall mean curvature. Between male and female otoliths of equal fish length, we found the mean curvature density curves to be more uniform for males. This implies a more smooth surface for male otolith surfaces.

Contents

Declaration of Authorship	i
Abstract	ii
Contents	iv
1 Introduction	1
1.1 European hake	1
1.2 Otoliths	1
1.2.1 Sulcus acusticus	3
1.2.2 Curvature	3
1.3 Data acquisition	4
1.3.1 Micro-CT scans	4
1.4 Research questions	8
1.5 Structure	8
2 Methods	9
2.1 Data transformation	9
2.1.1 Resizing	9
2.1.2 Aligning and rotating	10
2.1.3 Background removal	10
2.2 Analysis of the sulcus	12
2.2.1 Segmentation of the sulcus	13
2.2.1.1 Peak detection	14
2.2.1.2 Interpolation of peaks	16
2.2.1.3 Reconstruction of 2D sulcus surface	16
2.2.1.4 From 2D to 3D	17
2.2.2 Geometric measurements	18
2.2.2.1 Surface area	18
2.2.2.2 Volume	18
2.2.2.3 Error of estimation methods	19
2.2.3 Interface	19
2.2.4 Experiments	20
2.2.4.1 Total length and sulcus/otolith size	21
2.2.4.2 S : O ratio	22

2.3	Analysis of the curvature	22
2.3.1	Mean curvature	23
2.3.2	Preparing the otolith scans	23
2.3.2.1	Image stack transformations	23
2.3.2.2	Mesh transformations	24
2.3.2.3	Assessment of the mesh improvements	27
2.3.3	Detection of protuberances	27
2.3.4	Experiments	29
2.3.4.1	Total length and protuberances	29
2.3.4.2	Mean curvature and gender	30
3	Experiments and Results	31
3.1	Data transformation	31
3.2	Analysis of the sulcus	32
3.2.1	Sulcus segmentation	32
3.2.2	Geometric measurements	33
3.2.2.1	Comparison of volume estimates	33
3.2.3	Experiments	34
3.2.3.1	Surface area	34
3.2.3.2	Volume	37
3.3	Analysis of the curvature	38
3.3.1	Preparing the otolith scans	38
3.3.2	Detection of protuberances	40
3.3.3	Experiments	41
3.3.3.1	Protuberances and total length	41
3.3.3.2	Mean curvature and gender	41
4	Discussion	46
4.1	Analysis of the sulcus	46
4.1.1	Segmentation of the sulcus	46
4.1.2	Geometric measurements	46
4.1.3	Experiments	47
4.1.3.1	Surface area	47
4.1.3.2	Volume	48
4.2	Analysis of the curvature	49
4.2.1	Mean curvature derivation	49
4.2.2	Detection of the protuberances	49
4.2.3	Experiments	50
4.2.3.1	Total length and protuberances	50
4.2.3.2	Mean curvature and gender	50
5	Conclusion and Future Work	51
5.1	Analysis of the sulcus	51
5.2	Analysis of the curvature	52
5.3	Future work	53
5.3.1	Analysis of the sulcus	53
5.3.2	Analysis of the curvature	53

Bibliography	54
---------------------	-----------

Chapter 1

Introduction

1.1 European hake

The European hake is a teleost fish of the genus *Merluccius*. Hakes can reach a maximum length of 140 cm, a maximum weight of 14 kg, and the maximum age is estimated at 12 years [1].

The hake species is a major component of the demersal fish assemblages and is distributed over a wide depth range of 20 to 1000 meter throughout the Mediterranean Sea and the northeast Atlantic region [2]. The hake is an important predator of deeper shelf-upper slope Mediterranean communities and a valuable food resource for the human population of western Europe. Especially in Spain, the hake is popular, where over 700,000 tonnes of hake are imported annually [1].

Shorter hakes prefer to inhabit the sea at depths of 170 to 220 meters while larger hakes persist on the continental shelf with a preference for depths between 70 to 100 meters [3]. This migration is induced by a change in trophic requirements. During its early demersal life, the hake feeds on crustaceans. Subsequently, juvenile hakes migrate from the nursery areas to the parental stock, and when they reach a total length between 18 and 32 cm, they shift their diet towards small pelagic fish [4].

1.2 Otoliths

The otoliths, or ear stones, are organs within the inner ear of teleost fish. They serve as mechanoreceptors, processing acoustic, and postural information [5]. Otoliths are formed during embryo development and continue to grow in incremental layers of

CaCO_3 throughout the lifetime of the individual [6]. The growth and composition depend on physiological and environmental factors [7]. In combination with otoliths being metabolic inert, they are an important tool in marine and fisheries research as specifics of the physicochemical environment of the fish are recorded. Therefore, otoliths reveal time-keeping properties about the fish's biological history [8]. Furthermore, the otolith morphology is specific to species, populations, and stocks [9]. This allows the identification of a fish by studying the saccular otoliths.

The inner ears of the European hake contain three pairs of otoliths. The lapille and asterisci are correlated to the utricle and lagena end-organs which are associated with acoustic functions [10]. The sagitta, or the saccular otolith, is correlated to the saccule end-organ [11] which is associated with vestibular functions. The saccular otolith is the largest and has the highest morphological variability [11].

In Figure 1.1, the internal face, or proximal face, of a right saccular otolith of the European hake is visualized through a scanning electron microscope (SEM) [12]. In Figure 1.2, we zoom in on the otolith surface, which shows to be porous in the central region of the sulcus acusticus.

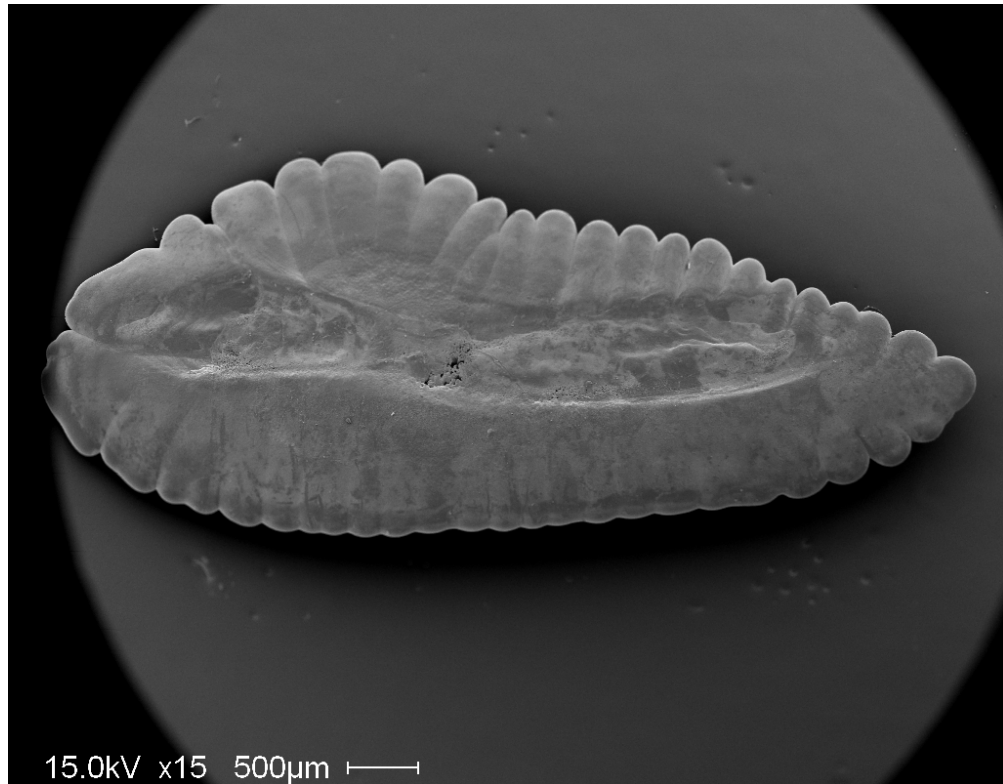


FIGURE 1.1: Internal face of a right saccular otolith of a European hake, obtained by a SEM.

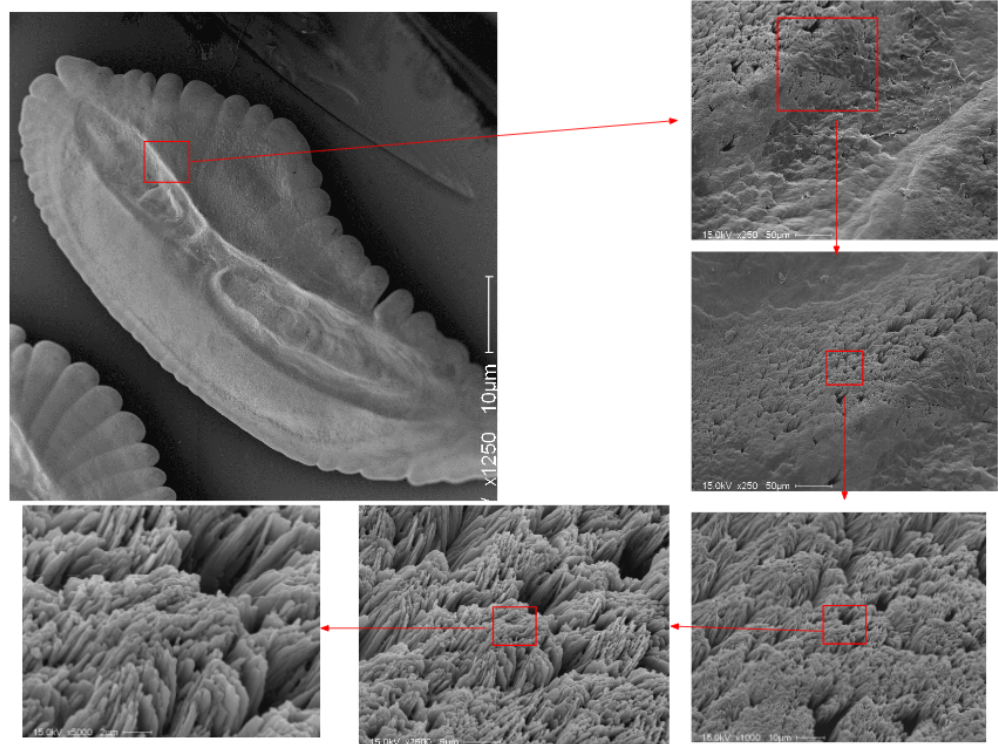


FIGURE 1.2: Surface of right saccular otolith of European hake, obtained by a SEM.

1.2.1 Sulcus acusticus

The internal face of the saccular otolith houses the sulcus acusticus, characterized by a groove [11]. The sulcus is an important anatomical structure since it is in contact with the sensory epithelium, or macula. For the majority of teleost fishes, including the hake, there exists a morpho-anatomical relation between the sulcus and the macula [13]. The sulcus size is therefore often used as a proxy for the size of the macula.

The ratio between the sulcus size and the total otolith size (S : O ratio) is correlated to habitat features such as water depth, diet, and mobility and has been found to vary among species [13]. Moreover, the S : O ratio influences the hearing abilities, where larger S : O ratios are linked to better hearing abilities [14].

1.2.2 Curvature

The morphology of the saccular otoliths changes as the hake ages. This is mostly noted by the formation of ridges and valleys on the otolith surface. Together, the ridges and valleys create touching branch-like structures, which are referred to as the protuberances [15]. The protuberances may have functional significance but have received little attention in literature [16].

The protuberances on the saccular otolith are mostly located on the perimeter and the external face, characterized by wrinkles on the surface (Figure 1.4). For otoliths of older hakes, we observe a lower presence of protuberances in comparison to otoliths of younger hakes, which look more smooth. The protuberances cover a large portion of the otolith surface and therefore have a significant influence on the otolith morphology and the curvature of the surface.

1.3 Data acquisition

During prior research, multiple European hakes are collected from the Western Adriatic Sea. For mature individuals, the sex is determined by macroscopic inspection of the gonads. Juvenile individuals have not reached sexual maturity and are labeled as indeterminate. For every individual, the total length is measured from mouth to tail with a digital caliper. Consequently, the juvenile fish have a length of 50-150 mm and adults have a length of 150-400 mm.

For nine female-male pairs of equal length, the right saccular otolith is extracted. In addition, the right saccular otolith is extracted for six juveniles of various lengths, resulting in a total of 24 extractions. Here, the right otolith is chosen arbitrarily since there is no side dimorphism between the saccular otoliths of the European hake.

For the extracted otoliths, the mass is estimated using a micro-scale. Thereafter, the otolith volume is estimated via the Buoyancy method. Finally, each fish-otolith pair is given a unique label to facilitate references. The label consists of the prefix “oto”, followed by a letter indicating the respective gender-group. The label ends with an arbitrary number.

In Table 1.1, we list the measurements and classifications of the fish-otolith pairs sorted on total length.

1.3.1 Micro-CT scans

The extracted saccular otoliths are digitized through a micro-computed tomography (micro-CT) scanner. Here, an x-ray beam transmits through the otolith samples creating a digital image. The gray-scale values in the images reflect the mean of the attenuation coefficient of the material [17]. Accordingly, materials with higher density have greater attenuation. By convention, higher density pixels are white while the absence of material is reflected by black pixels.

TABLE 1.1: Fish-otolith pairs.

Label	Gender	Total length (mm)	Otolith volume (mm^3)
otoI48	I	50	0.22
otoI47	I	82	1.12
otoI96	I	96	1.88
otoI59	I	101	2.22
otoI89	I	115	3.40
otoI9	I	130	5.07
otoF75	F	164	8.80
otoM30	M	164	10.16
otoF176	F	182	11.26
otoM78	M	182	12.99
otoF200	F	192	12.79
otoM145	M	192	14.74
otoF11	F	221	17.84
otoM203	M	221	20.55
otoF34	F	232	20.02
otoM19	M	232	23.05
otoF198	F	244	22.56
otoM150	M	244	25.96
otoF83	F	268	28.17
otoM229	M	268	32.40
otoF73	F	300	36.80
otoM278	M	300	42.28
otoF177	F	400	72.73
otoM257	M	400	83.39

The otoliths are scanned in groups of two to three to reduce scanning time. In addition, the groups are multi-sampled which means that for each group, multiple scans are made which after that are stitched together. Consequently, most of the otolith scans contain artificial interruptions on their surfaces, as demonstrated by Figure 1.3.

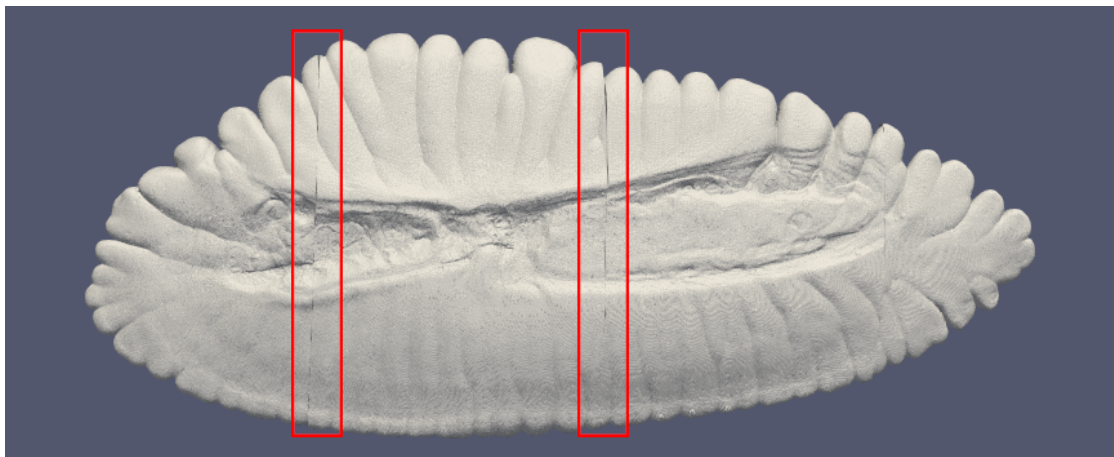


FIGURE 1.3: Interruptions on internal face of otoF200, emphasized by red-lined boxes.

TABLE 1.2: Specifications of the supplied otolith image stacks.

Label	Number of images	Image size (pixels)	Ψ (μm)
otoI48	992	206×534	2.02
otoI47	2197	462×901	2.02
otoI96	2756	1100×1320	2.02
otoI59	2567	930×690	2.02
otoI89	2997	1252×401	2.02
otoI9	3146	1178×871	2.02
otoF75	3552	346×299	2.53
otoM30	3518	537×1798	2.38
otoF176	3428	573×1542	2.38
otoM78	3657	644×1686	2.38
otoF200	3830	1008×1498	2.38
otoM145	3891	1733×788	2.38
otoF11	4207	2037×886	2.38
otoM203	2924	1220×566	3.69
otoF34	3140	1381×700	3.69
otoM19	3196	1480×910	3.33
otoF198	3244	1254×756	3.69
otoM150	3426	1522×1096	3.33
otoF83	1605	629×287	8.33
otoM229	3511	459×1515	3.69
otoF73	3100	1334×371	4.76
otoM278	4045	512×1677	3.69
otoF177	2100	554×842	8.33
otoM257	3882	1705×589	4.76

To partition each otolith into an individual representation, segmentation is performed. The resulting representations are supplied as stacks of two-dimensional TIFF images. Each image, or slice, represents a cross-section of the otolith volume. Stacking the slices adds a third dimension yielding a 3D representation [18]. This transforms the pixels into isotropic voxels, where slice thickness Ψ_z is equal to the width Ψ_x and height Ψ_y of a pixel.

The specifications of the image stacks are shown in Table 1.2.

In Figure 1.4, we visualize the reconstructed surface of a right saccular otolith for a juvenile, female, and male hake. The upper row shows the internal face, including the sulcus. The bottom row shows the external face of the otoliths. A comparison between the otoliths demonstrates the external face and perimeter of the mature otoliths to be less smooth due to a higher presence of protuberances.

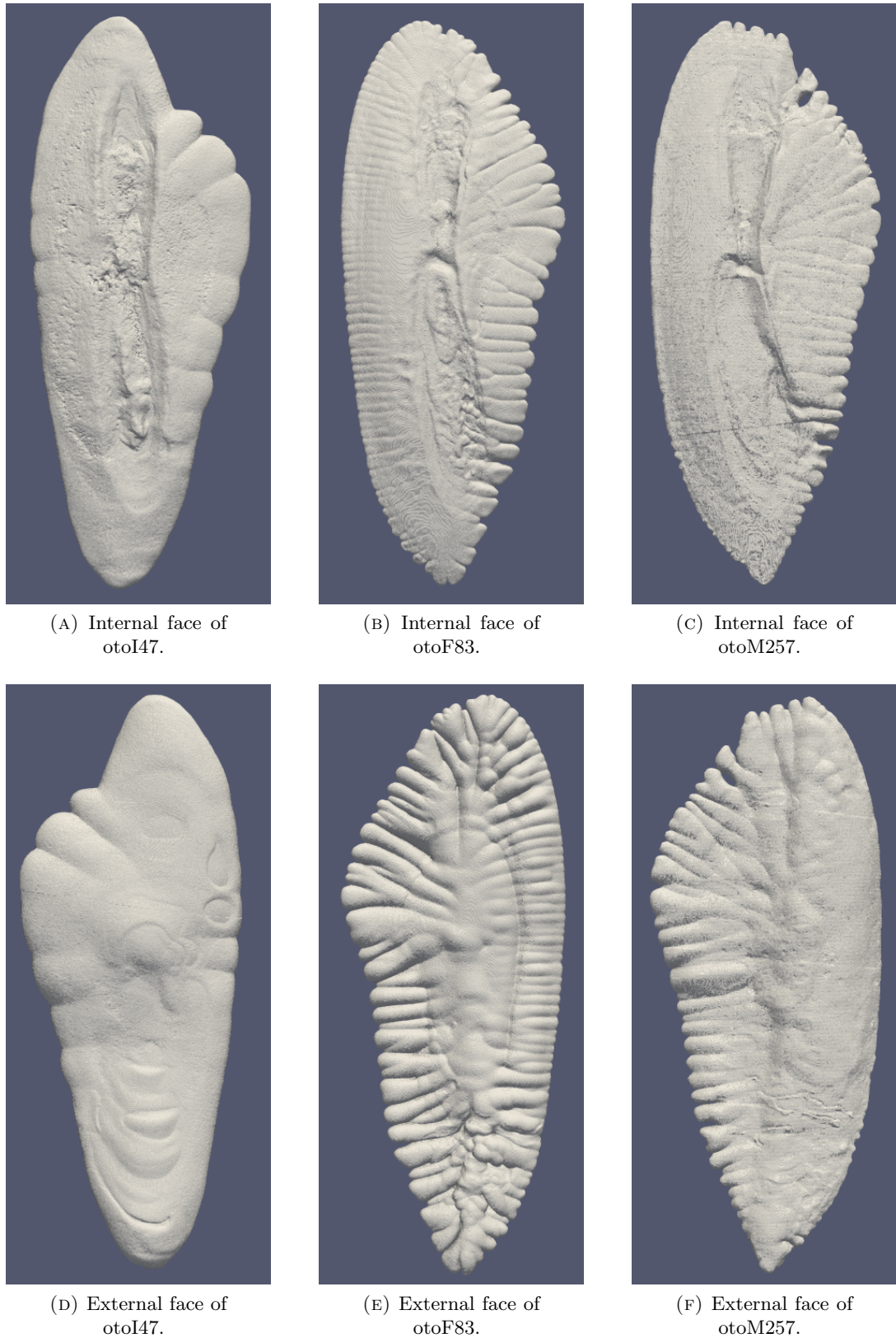


FIGURE 1.4: Surface reconstruction (Marching Cubes) for right saccular otoliths, visualized with ParaView.

1.4 Research questions

The S : O ratio presumably influences the hearing abilities of the fish. However, the effects of the ratio have not been researched extensively since it is difficult to reliably quantify the dimensions of the sulcus [19].

In Lombarte [20], the S : O relation is examined for the *Merluccius capensis* and *Merluccius paradoxus*. To ascertain whether their findings apply to European Hake, *Merluccius merluccius*, we examine the micro-CT scans containing 24 right saccular otoliths of hakes. This introduces the following research question:

RQ 1: How does the saccular sulcus size relate to the saccular otolith size for the European hake?

Thereafter, we examine the otolith curvature and the protuberances using the micro-CT scans. We investigate the change in curvature as the fish ages, which we capture by the following research question:

RQ 2: How does the curvature of the saccular otolith of the European hake change over time?

1.5 Structure

In the subsequent chapters, we present the methods used and experiments performed to answer our research questions (chapter 2). Thereafter, we demonstrate the results of the experiments (chapter 3) and interpret the corresponding results (chapter 4). Finally, we conclude our findings and propose future work (chapter 5).

Throughout this thesis, we make a distinction between the sulcus analysis, which focuses on RQ1, and the curvature analysis, which focuses on RQ2.

Chapter 2

Methods

In this chapter, we present our methods. The content of this chapter is divided into three parts. First, we preprocess the micro-CT scans of the otoliths (section 2.1). Subsequently, we use the transformed scans to analyze the sulcus (section 2.2) aiming to find an answer to RQ1. Finally, we analyze the otolith curvature through the transformed scans to find an answer to RQ2 (section 2.3).

2.1 Data transformation

The micro-CT scans are supplied as TIFF image stacks. To facilitate future analyzes concerning the sulcus and curvature, we apply several transformations to the stacks. We achieve this using Python3, in combination with libraries the Visualization Toolkit (VTK) [21], OpenCV [22] and NumPy [23].

2.1.1 Resizing

The amount of images and the image size varies per stack (Table 1.2). In addition, the voxel size differs per scan, which results in the stack sizes ranging from 120 MB to 12,000 MB. Due to memory restrictions, we are unable to process such sizable stacks on our local machine. Via a remote server with sufficient computational power, we reduce the stack sizes through uniform resampling [24] with linear interpolation. We set magnification factor $\omega \in [0.0, 1.0]$ such that the resulting image stack contains a maximum of 2,000 slices. We allow one decimal for ω to reduce errors during the later performed geometric measurements.

2.1.2 Aligning and rotating

The orientation of the otoliths in the image stacks is inconsistent. This is caused by the otoliths being positioned arbitrarily into the micro-CT scanner to be able to fit multiple otoliths simultaneously. To obtain a consistent orientation among the scans, we choose to align the axes of all digital otolith volumes to the axes of the Cartesian coordinate system. We algorithmically derive the transformation matrix that accomplishes the desired rotation. This is preferable to the manual derivation of rotation angles since it improves consistency in the orientation.

First, we derive the current orientation of the digital otolith through the oriented bounding box (OBB). This is the smallest box that completely encloses the otolith volume [25]. Subsequently, we define a mapping to describe how the axes of the OBB should align with the axes of the coordinate system:

- the OBB's shortest axis $O\vec{B}B_{min}$ should align with the Cartesian y -axis,
- the OBB's middle axis $O\vec{B}B_{mid}$ should align with the Cartesian x -axis,
- the OBB's longest axis $O\vec{B}B_{max}$ should align with the Cartesian z -axis.

We then transform the OBB axes into unit vectors. Together they form the columns of transformation matrix T , in accordance with the mapping:

$$T = \begin{bmatrix} O\hat{B}B_{mid} & O\hat{B}B_{min} & O\hat{B}B_{max} \end{bmatrix}^{-1}. \quad (2.1)$$

The original orientation of the otolith in the scan determines whether the internal side of the newly aligned otolith is faced upwards or downwards. For the sulcus analysis, it is beneficial that the internal side, housing the sulcus, is faced upwards. If this is not the case, we apply an additional rotation of 180° in the xy -plane to the concerning stack.

In Figure 2.1, we illustrate the orientation of a digital otolith after alignment and rotation is applied. It shows the otolith OBB to be aligned to the axes of the coordinate system and the internal side to be faced upwards.

2.1.3 Background removal

OtoF75, otoM229, otoM278, otoM30, and otoM78 are scanned with tissues wrapped around the otoliths to prevent them from touching. Consequently, the backgrounds in the particular scans are non-empty (Figure 2.2a) which is disadvantageous for the sulcus

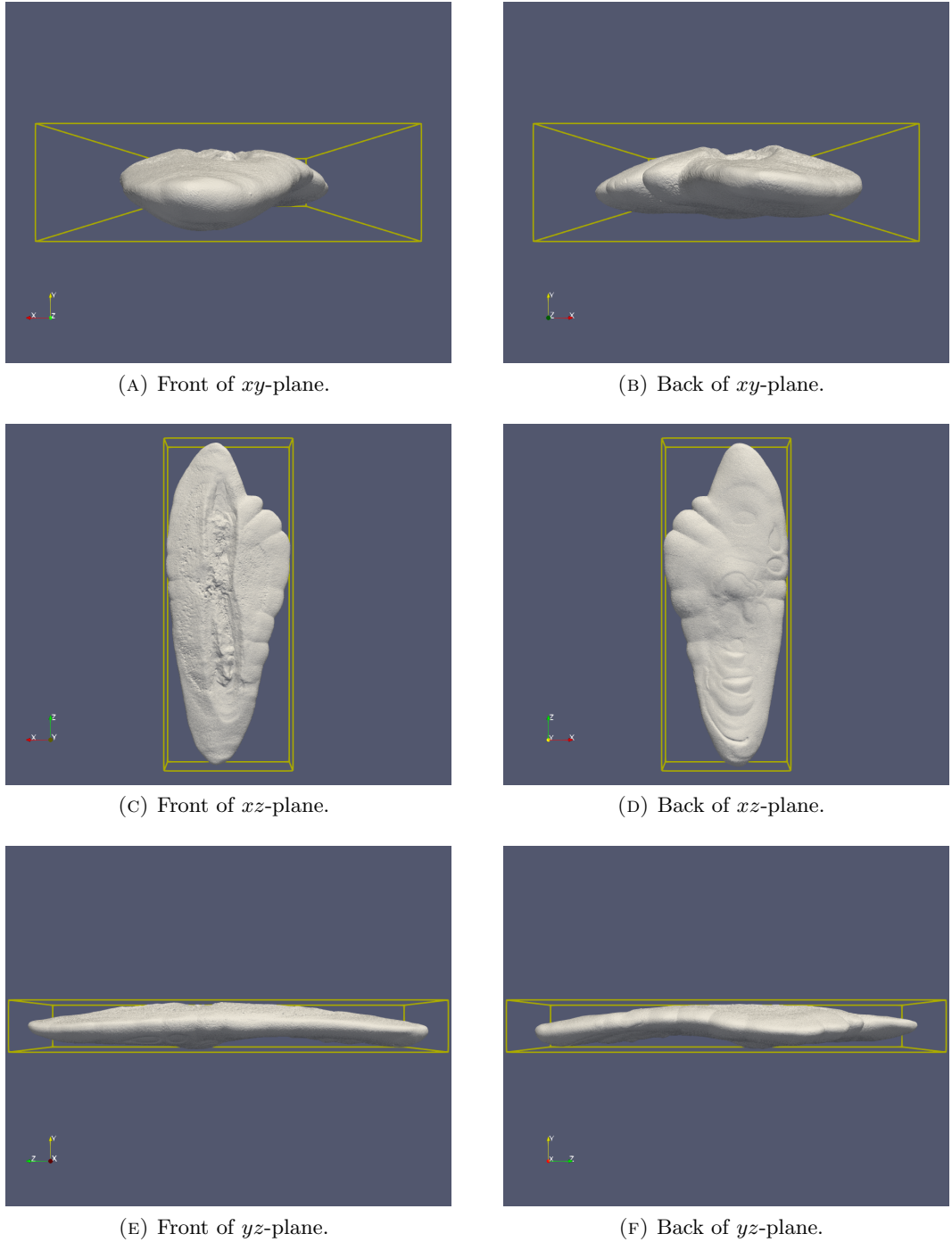
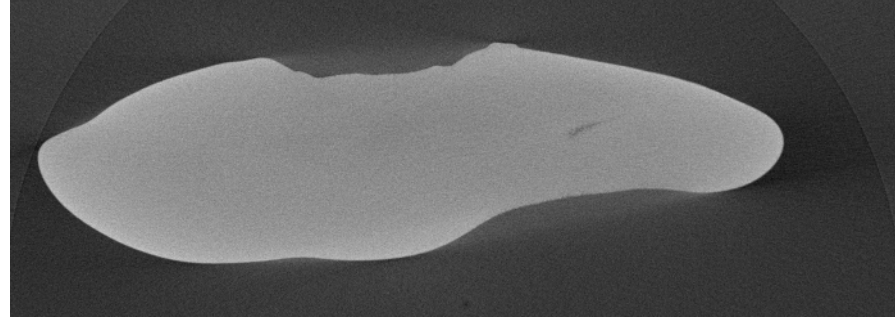


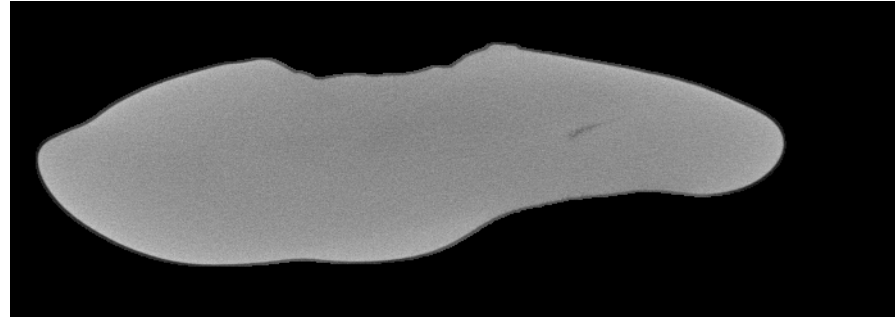
FIGURE 2.1: Orientation of otoi48 after alignment and rotation.

analysis. To remove the background, we derive the two-dimensional contour for every slice in the image stacks through OpenCV. The contour serves as a mask, to which we apply dilation with kernel size $n = 3$. The expansion of the mask includes pixels around the otolith contour that incorporate the anti-alias property. These pixels provide important information on the detail of the edges and their inclusion reduces distortion artifacts during the later applied volume rendering. Subsequently, we remove the pixels

outside of the acquired mask resulting in an empty background (Figure 2.2b).



(A) Original (non-empty) background.



(B) After background removal.

FIGURE 2.2: Background removal in slice 815 of otoF75.

In Figure 2.3 we show an overview of the applied transformations.

2.2 Analysis of the sulcus

We analyze the sulcus acusticus in the transformed otolith scans to find an answer to our first research question:

RQ 1: How does the saccular sulcus size relate to the saccular otolith size for the European hake?

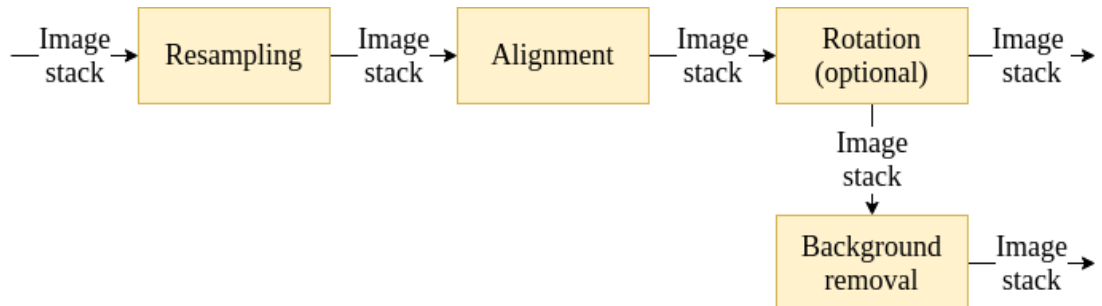


FIGURE 2.3: Applied image stack transformations.

To measure the sulcus size, we detach the sulcus from the otolith scans (section 2.2.1). Subsequently, we use the partitioned sulcus to estimate the volume and surface area (section 2.2.2). Using the obtained measurements we perform several experiments (section 2.2.4) related to characteristics of the fish-otolith pair (Table 1.2) with which we aim to answer the research question.

The code to segment, measure and analyze the sulcus is written in Python3 using libraries as discussed in section 2.1. Additionally, we use packages as pandas [26], matplotlib [27] to create plots and TKinter [28] to develop an interface.

2.2.1 Segmentation of the sulcus

Conventional segmentation methods partition digital images into segments based on edges [29] or density [30]. These methods are unsuitable to segment the sulcus due to its complex morphology. The sulcus is a groove making it is problematic to determine the edges. In addition, its density is equal to zero. Another possibility to segment the sulcus concerns watershed segmentation, which partitions images based on different catchment basins [31]. However, the sulcus cannot be enclosed by a single plane, making watershed segmentation also unsuitable.

To overcome the lack of applicable methods, we develop a semi-automated segmentation method to partition the sulcus. Our method relies on the earlier established orientation of the digital otolith, which ensures the internal side of the otolith to be located in the top part of the xz -plane (Figure 2.1c). This attribute allows us to segment the sulcus in a single slice. Subsequently, we obtain a 3D segmentation by repeating the process for a consecutive series of slices.

First, we transform the top part of the otolith surface in a slice to one-dimensional signal E . The derivation of E is straight-forward and is achieved by iterating over the columns of an image/slice. For every column, we take the appurtenant lowest y -value that contains a non-empty pixel:

$$E = \{y_{max}(x_1), y_{max}(x_2), \dots, y_{max}(x_N)\}, \quad (2.2)$$

Note that by convention, the origin of digital images is located in the bottom left, as opposed to the origin of the Cartesian coordinate system.

2.2.1.1 Peak detection

Generally, the peaks on E can be used to describe the boundaries of the sulcus, as illustrated by Figure 2.4a. Consequently, the derivation of the E 's peaks allows us to obtain a 2D segmentation of the sulcus, as shown by Figure 2.4b.

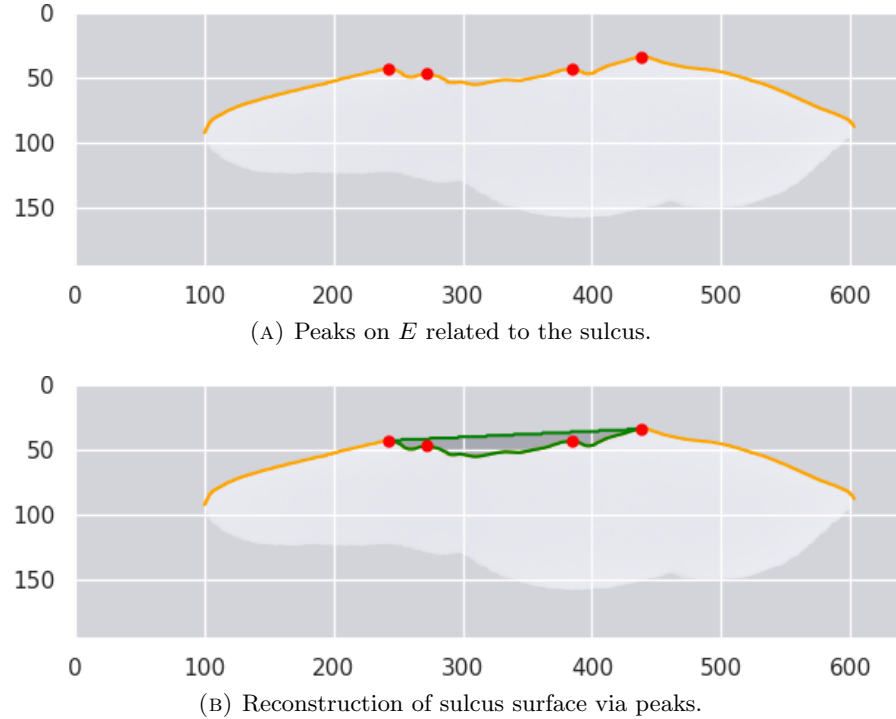


FIGURE 2.4: 2D segmentation of the sulcus (slice 600 of otoF83).

We algorithmically derive the peaks of E through SciPy's [32] peak detection algorithm. Considering not all detected peaks are related to the sulcus, we separate the detected peaks into sulcus peaks and noise peaks. For the sulcus peaks, we ignore the intermediate peaks as the leftmost and rightmost peaks are sufficient to describe the boundaries of the sulcus. Noise peaks are, therefore, only detrimental when they are positioned outside these boundaries.

We characterize three different types of noise peaks:

1. Besides the sulcus, the saccular otolith contains an additional groove called the crista. The crista is located next to the sulcus and therefore induces peaks on E in multiple slices. Typically, some peaks of the crista are shared with the sulcus. The remaining crista peaks are considered to be noise.
2. At the posterior and anterior proportion of the image stack, lengthwise protuberances interfere with the sulcus. Consequently, this creates noise peaks in the corresponding slices.

3. The interruptions caused by the stitching process, create sharp edges in the otolith slices which are detected as peaks. Since they are not part of the sulcus, we label them as noise.

Peaks induced by the crista and protuberances are less pronounced in comparison to the sulcus peaks. Hence we can reduce their presence by smoothing of E , which we achieve through the Savitzky-Golay-filter [33]. This filter fits consecutive sets of adjacent points with a n -th order polynomial via linear least squares. Window length m specifies the distance between two points to be considered adjacent, essentially being a smoothing factor. We manually determine a suitable value for m per scan such that the smoothing reduces the detection of noise peaks while most sulcus peaks are preserved.

An example of the effect of smoothing of E on the detection of peaks is visualized in Figure 2.5.

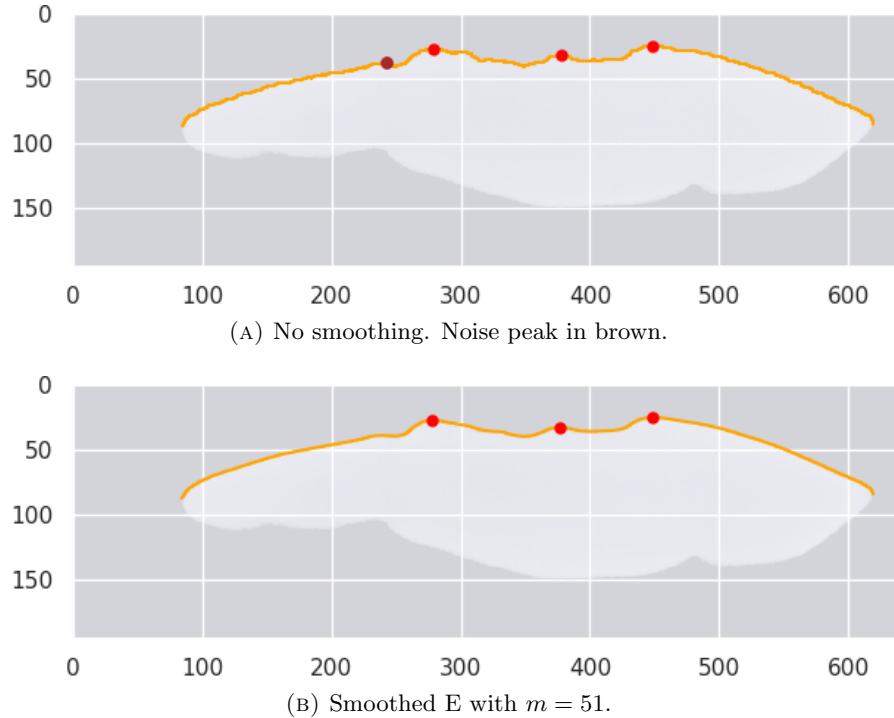


FIGURE 2.5: Peak detection on E (slice 867 of otoF83).

The smoothing only achieves its intended effect when the noise peaks are significantly smaller than the sulcus peaks. Alternatively, noise peaks caused by the interruptions are generally more pronounced than the sulcus peaks. For such noise peaks, smoothing is not sufficient. As a solution, we include the option to manually add and adjust detected peaks. The introduction of the manual component allows us to increase the accuracy of the segmentation but also introduces a bias. Furthermore, we note that for some peaks, it is rather difficult to manually analyze whether they should be considered noise in the 3D representation of the sulcus.

2.2.1.2 Interpolation of peaks

The sulcus is present in the majority of slices, leading to substantial amounts of slices that need examination on the location of sulcus peaks. Additionally, the shape of the otolith and hence the sulcus differs only slightly between consecutive slices. Given these conditions, we include the option to reconstruct the sulcus peaks for slice s through linear interpolation.

To apply interpolation to s , we need the leftmost and rightmost sulcus peak of two neighboring slices. We delimit the maximum distance between slice s and another slice to be considered neighbors by n . In other words, there should be at least one slice in the range of $[s - n, s - 1]$ (down neighbor) and in the range of $[s + 1, s + n]$ (up neighbor) with pre-detected sulcus peaks. If this applies, we can interpolate the x -coordinate of the k -th sulcus peak of s :

$$x_k = x_k^D + (x_k^U - x_k^D) \cdot \frac{d^D}{d^D + d^U}, \quad (2.3)$$

with x_k^D and x_k^U being the x -coordinate of the k -th peak of the down and up neighbor respectively. d^D and d^U are the corresponding distances to these neighbors. We recall that $k \in [1, 2]$ since we only interpolate the leftmost and rightmost sulcus peaks. Finally, the y -coordinate of the interpolated peak is derived by taking the corresponding y -value for x_k on E in s .

2.2.1.3 Reconstruction of 2D sulcus surface

We can now describe the interior of the sulcus in a slice through E bounded by the acquired sulcus peaks. To obtain a 2D representation of the sulcus, we must derive an enclosing part that serves as the exterior of the sulcus. We acquire this part using the following procedure:

1. We draw a pixelated line [34] between the sulcus peaks with the lowest and highest x -coordinate (Figure 2.6a and Figure 2.6b).
2. The point of E that crosses the line with the highest vertical distance is added to the line (Figure 2.6b and Figure 2.6c).
3. Repeat step 2 until no more points of E cross the line.

Together, the derived interior and exterior of the sulcus describe the sulcus circumference in a slice. By filling in the pixels within the circumference, we obtain the sulcus surface (Figure 2.6d).

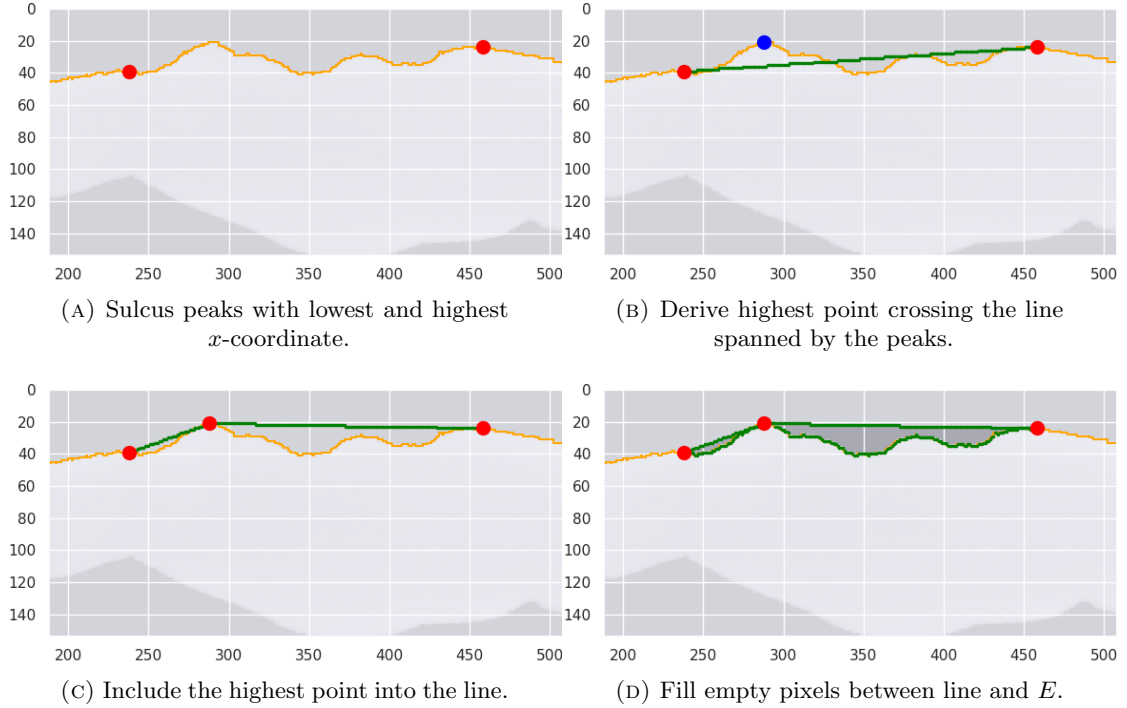


FIGURE 2.6: Reconstruction of sulcus surface in slice 794 of otoF83.

2.2.1.4 From 2D to 3D

We obtain a 3D segmentation of the sulcus by applying the above-described procedure to all slices in an otolith image stack. For this, we use the following strategy:

1. First, we detect sulcus peaks using two detection loops. The first loop starts in the middle slice and iterates to the first slice with an increment of $-l$. The second loop starts in the middle slice + 1 and iterates to the last slice with an increment of l .
2. For the encountered slices, we detect the sulcus peaks. If for k consecutive increments less than two sulcus peaks are detected, the loop terminates prematurely.
3. After the termination of both detection loops, we manually verify and adjust the detected sulcus peaks as needed.

4. If $l > 1$, we end up with slices that have no detected sulcus peaks while their neighbors do. To these slices, we apply interpolation to derive their sulcus peaks. Here it is important that $l < n$.

By setting $l > 1$ we improve efficiency since the peak detection algorithm is time-consuming. On the other hand, the interpolation can reconstruct sulcus peaks with high precision due to the similar morphology of the otolith in nearby slices.

5. Finally, we reconstruct the sulcus surface in every slice using the acquired sulcus peaks.

2.2.2 Geometric measurements

The obtained 3D representations of the sulci allow us to perform 3D geometric measurements such as the surface area and volume.

2.2.2.1 Surface area

To estimate the surface area of the sulci and otoliths, we transform the corresponding image stacks into triangular meshes. We generate these meshes using Marching Cubes [35] which is arguably the most used algorithm to reconstruct surfaces of image data. We note that while the meshes are highly accurate approximations of the surfaces in the stacks, they still introduce a small error [36].

For every mesh R , we obtain the surface area $S(R)$ by aggregating the areas spanned by the individual triangles in the mesh. The mesh is not bounded to the voxel grid hence $S(R)$ is expressed as a portion of the pixels. To express $S(R)$ metrically, we multiply the portion by the metric area of an individual pixel:

$$S = S(R) \cdot (\Psi \cdot \omega)^2, \quad (2.4)$$

where Ψ is the voxel resolution (Table 1.2) and ω the magnification factor used during the resampling.

2.2.2.2 Volume

Like the surface area, we estimate the volume of the sulci and otoliths through the corresponding triangular meshes. For mesh R we derive its volume $V(R)$ by determining

the portion of voxels that R is occupying [37]. To derive a metric volume measurement, $V(R)$ is multiplied by the metric volume of an individual voxel:

$$V = V(R) \cdot (\Psi \cdot \omega)^3. \quad (2.5)$$

During prior research, the otolith volume is estimated manually (see Table 1.2). This allows us to make a comparison between the (metric) digital otolith volume estimation $V = V_{digital}$ and the manual otolith volume estimation V_{manual} . Since both estimations likely contain an error, we compare them by the relative percent difference:

$$\text{Percent difference} = \frac{|V_{manual} - V_{digital}|}{\frac{V_{manual} + V_{digital}}{2}} \times 100. \quad (2.6)$$

2.2.2.3 Error of estimation methods

To assess the inaccuracy of our estimation methods, we apply them to sphere meshes. This allows us to derive an error considering the sphere surface area is analytically derived via $4\pi \cdot r^2$, and the sphere volume via $\frac{4}{3} \cdot \pi \cdot r^3$.

The sphere meshes are obtained by applying Marching Cubes to various image stacks that contain sphere volumes of different r . The slices in a stack contain rasterized binary circles [38]. To allow Marching Cubes to interpolate on the edges, we apply 3D Gaussian smoothing ($\sigma = 3$) to stacks, resulting in a more continuous mesh (Figure 2.7).

In Figure 2.8 we demonstrate the observed percent errors:

$$\text{percent error} = \frac{|X_{numerical} - X_{analytical}|}{X_{analytical}} \times 100, \quad (2.7)$$

where $X_{numerical}$ is the value obtained through the estimation methods and $X_{analytical}$ the analytical derived value. The percent error for both methods is under 1% making the inaccuracy of both estimation methods negligible.

2.2.3 Interface

We incorporate the functionality concerning the segmentation of the sulcus and the geometric measurements into a graphical user interface (GUI), visualized in Figure 2.9. The objective of the GUI is to allow the user to use the functionality without the

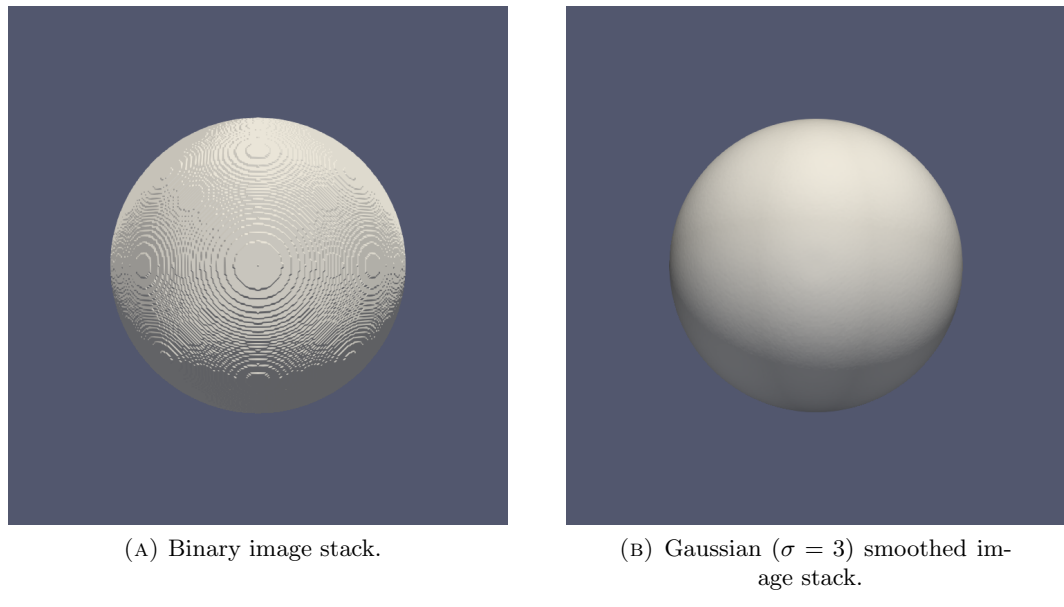


FIGURE 2.7: Mesh generation of sphere via Marching Cubes of image stack.

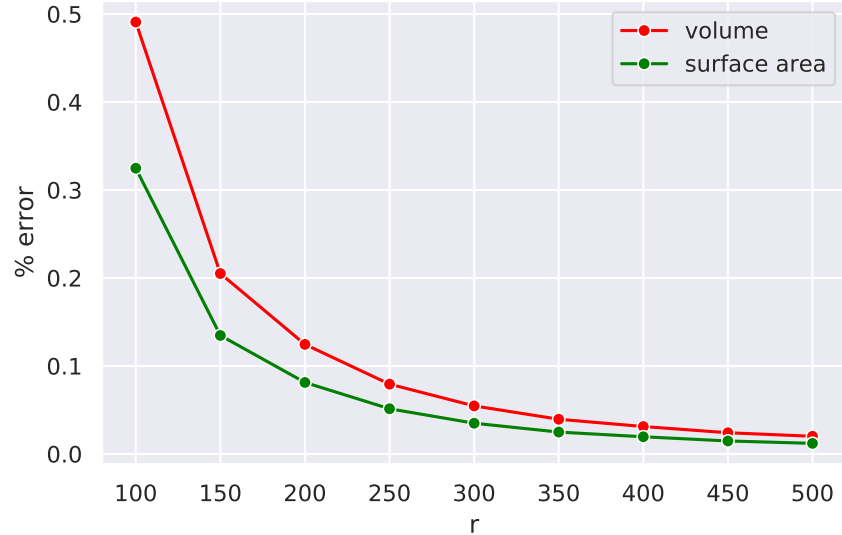


FIGURE 2.8: Percent error for geometric estimations of Marching Cubes sphere meshes with various r .

adjustment of any code. In addition, the GUI provides the visual component for the manual adjustment and verification of the automatically detected peaks.

2.2.4 Experiments

To find an answer to our research question, we perform three experiments to examine the sulcus and otolith of the European hake, *Merluccius merluccius*. Here we replicate

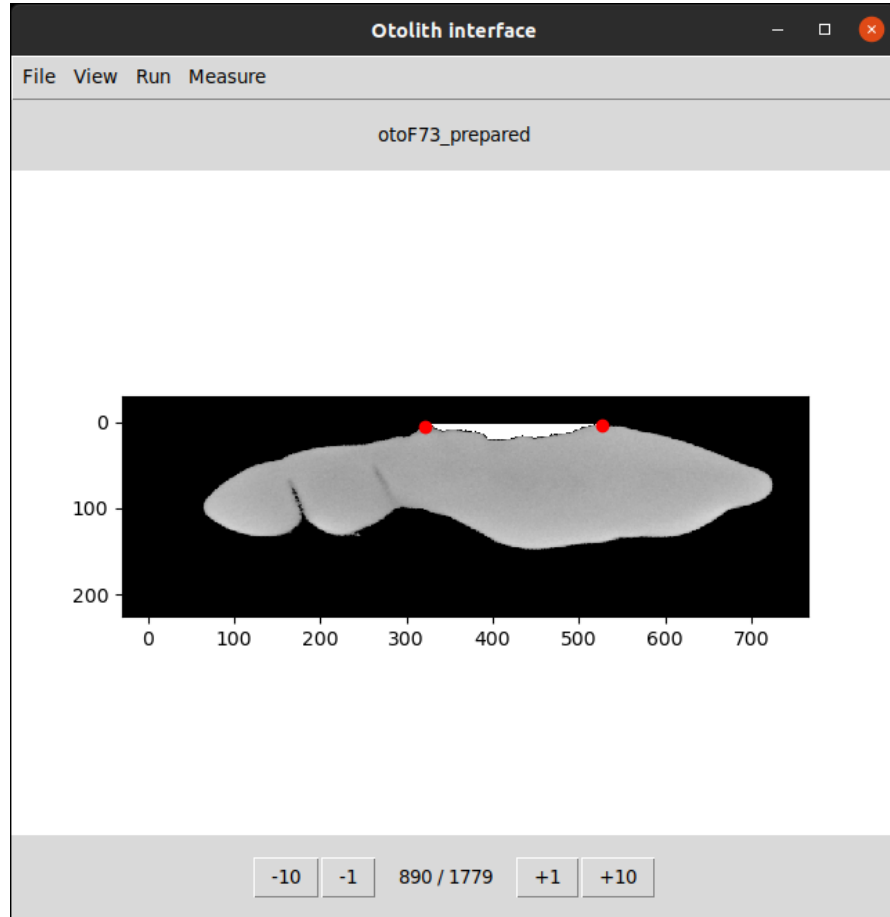


FIGURE 2.9: Interface on Ubuntu 20.04.

the experiments performed by Lombarte [20] who study the sulcus size relative to the otolith size ($S : O$ ratio) for the *Merluccius capensis* and *Merluccius paradoxus*.

In Lombarte [20], 2D images of the otolith's proximal face are used hence the $S : O$ ratio is expressed through the proximal surface area of the sulcus and otolith. Since we have 3D representations of the sulci and otoliths, our measurements include the entire surface area. Additionally, we also express the size by the obtained volume estimates. Throughout our experiments, we, therefore, separate the $S : O$ ratio into the $SSA : OSA$ ratio, which concerns the surface area estimates, and the $SV : OV$ ratio, concerning the volume estimates.

2.2.4.1 Total length and sulcus/otolith size

Currently, there exists no method to derive the age of the hake accurately [39]. During our experiments, we use the total length of the individuals as an age indication as on average older hakes are longer. Plotting of the total length against the sulcus size allows us to examine the sulcus growth relative to age. Subsequently, we also plot the total

length against the otolith size. We use regression to fit the equations and determine the goodness of the fits by the coefficient of determination R^2 :

$$R^2 = 1 - \frac{SSR}{SST}, \quad (2.8)$$

where SSR is the sum of squares of the residuals and SST the sum of the quadratic deviations from the mean.

2.2.4.2 S : O ratio

To answer RQ1, we plot the sulcus size relative to the total otolith size. Thereafter, we explore the distribution of the S : O ratio per gender to emphasize a potential sex dimorphism. Finally, we plot the total length against the S : O ratio.

Shorter and younger hakes prefer to inhabit the sea at deeper sea levels [3] in comparison to longer and older hakes. Living at deeper sea levels reduces vision making the individual more dependent on hearing abilities to navigate [40]. Therefore, we expect to find greater S : O ratios for juvenile hakes as this is linked to better hearing abilities [14].

2.3 Analysis of the curvature

The surfaces of mature otoliths contain more protuberances in comparison to juvenile otoliths, as demonstrated by Figure 1.4. We assume this is the effect of sound waves passing through the otoliths. Naturally, as the fish ages, more sound waves reach the otoliths. To elaborate on the curvature of the saccular otoliths, we formulate the following research question:

RQ 2: How does the curvature of the saccular otolith of the European hake change over time?

To derive an accurate and meaningful representation of the mean curvature on the otolith scans, we apply additional transformations to otolith scans (section 2.3.2). Thereafter, we develop a method to localize the tops of the observed protuberances on the otolith perimeter (section 2.3.3). Finally, we perform experiments regarding the mean curvature and detected protuberances to find an answer to the research question.

The code to derive the mean curvature and detected and analyze the protuberances is written in Python3 using libraries as discussed in section 2.2. Additionally, we use scikit-learn [41] and Meshlab [42].

2.3.1 Mean curvature

The mean curvature H is an extrinsic measure of curvature, describing the local curvature of a surface. In point p , $H(p)$ can be derived by taking the average of its principal curvatures k_1 and k_2 , which are the minimum and maximum curvature in p respectively. The sign of $H(p)$ is positive if the surface in p is convex. Alternatively, $H(p)$ is negative when the surface is concave.

The derivation of H allows us to assess the extent of the curvature distribution for the otolith scans. Additionally, through H we can localize the tops of the protuberances as the tops consist of multiple vertices where $H(p) > 0$. Moreover, the tops are separated by valleys which are characterized by vertices where $H(p) < 0$.

2.3.2 Preparing the otolith scans

To derive H for the otoliths, we transform the scans into triangular meshes via Marching Cubes. Sequentially, we derive H for every vertex in the mesh [43] [44].

In Figure 2.10a we visualize the result of this procedure where different values of H are denoted by color. It shows a grain textured surface, which we partly attribute to the actual otolith surface being porous (Figure 1.2). However, for most scans, the resolution of the micro-CT scanner is not high enough to register all porosity. In addition, the grain is the result of the otolith scans being discretized approximations of the actual otoliths. It is therefore undetermined to what extent the texture is artificial.

The grain texture disrupts the clarity of the distribution of H on the otolith surface. To derive a more correct and accurate H , we apply additional transformations to the scans. We make a distinction between transformations applied to image stacks and transformations applied to the corresponding meshes.

2.3.2.1 Image stack transformations

To diminish the grain, we apply Gaussian smoothing to the image stacks. The smoothing inevitably deforms the otolith surface, hence we limit the magnitude by $\sigma = 3$.

In Figure 2.10, we visualize the generated mesh of a Gaussian smoothed otolith image stack. The figure illustrates a considerable improvement in continuity of the distribution of H , with large regions that possess continuous values.

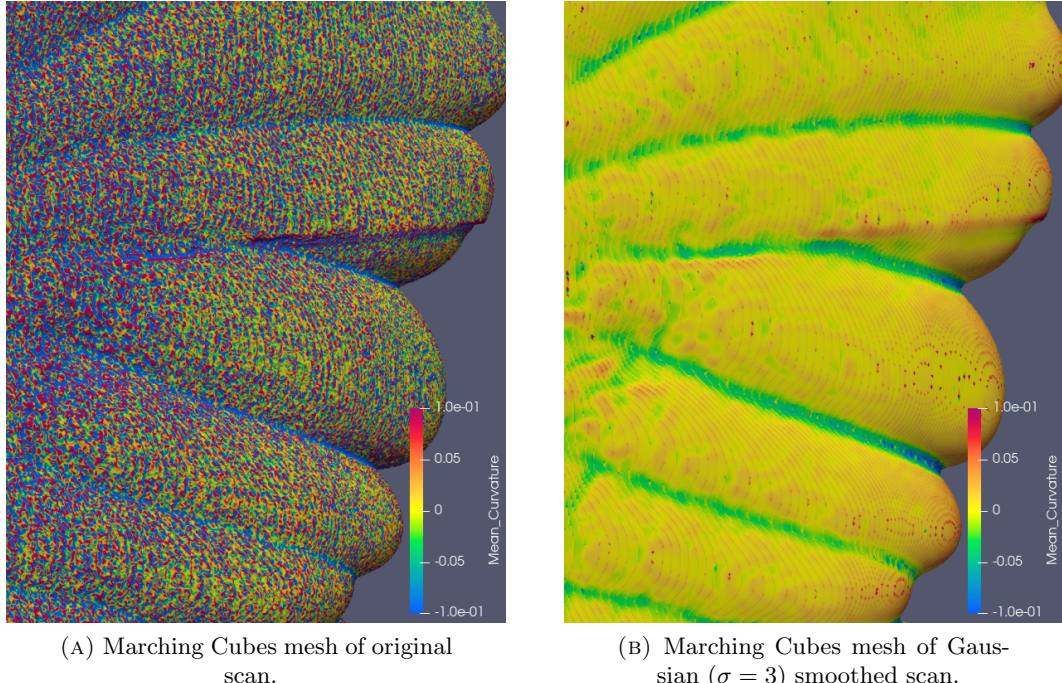


FIGURE 2.10: H on otoF73 mesh.

2.3.2.2 Mesh transformations

The Marching Cubes meshes of the smoothed image stacks display artifacts, observed in the form of ring-like structures on the surfaces (Figure 2.10b). These artifacts are caused by the discretization taking place when the otoliths are scanned. Subsequently, Marching Cubes uses linear interpolation to estimate the position on the edge. Since the actual otolith surface is described by a non-linear implicit function, the interpolated positions are poor estimates of the actual position on the edge [36].

To examine the ring-like structures, we generate a sphere mesh by applying Marching Cubes to a Gaussian ($\sigma = 3$) smoothed image stack containing a sphere with $r = 100$. Once again, the sphere allows us to derive an error for the acquired H values as a sphere is a constant-mean-curvature surface where $H = \frac{1}{r}, \forall p$. The result is demonstrated in Figure 2.11, which shows the error of H to be substantial throughout the surface (Figure 2.11c). Via the distribution plot of H (Figure 2.11d), we find the values to be in the range $[-0.10, 0.10]$. The average H is 0.0124, with a standard deviation of 0.0387.

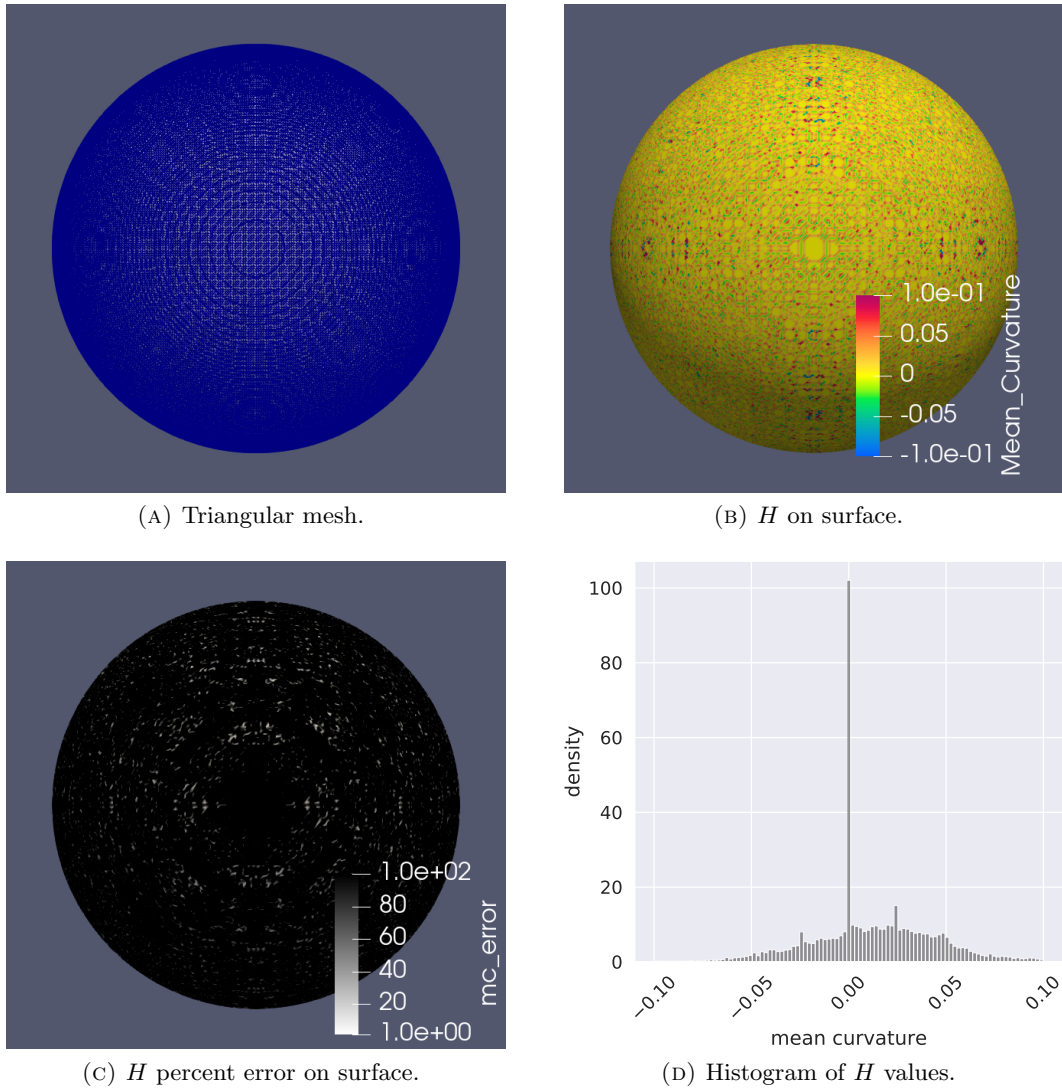


FIGURE 2.11: H for sphere mesh with $r = 100$. Mesh generated via Marching Cubes.

To put the inaccuracy into perspective, we create an alternative sphere mesh by subdividing an icosahedron multiple times [45]. This resembles an ideal construction of a sphere through triangles. In Figure 2.12, we show the derivation of H for this mesh. It shows a continuous and constant distribution of H . Logically, the average H in this mesh is 0.010, with a standard deviation of 0.

A comparison between Figure 2.11 and Figure 2.12 emphasizes the importance of the mesh topology on the accuracy of H . However, to reconstruct a mesh of the otoliths, we are bound to a surface reconstruction algorithm such as Marching Cubes. To derive a more accurate H , we, therefore, improve the topology of the Marching Cubes meshes through the application of several filters. Here the applied filters must preserve the original boundaries of the otolith mesh as much as possible.

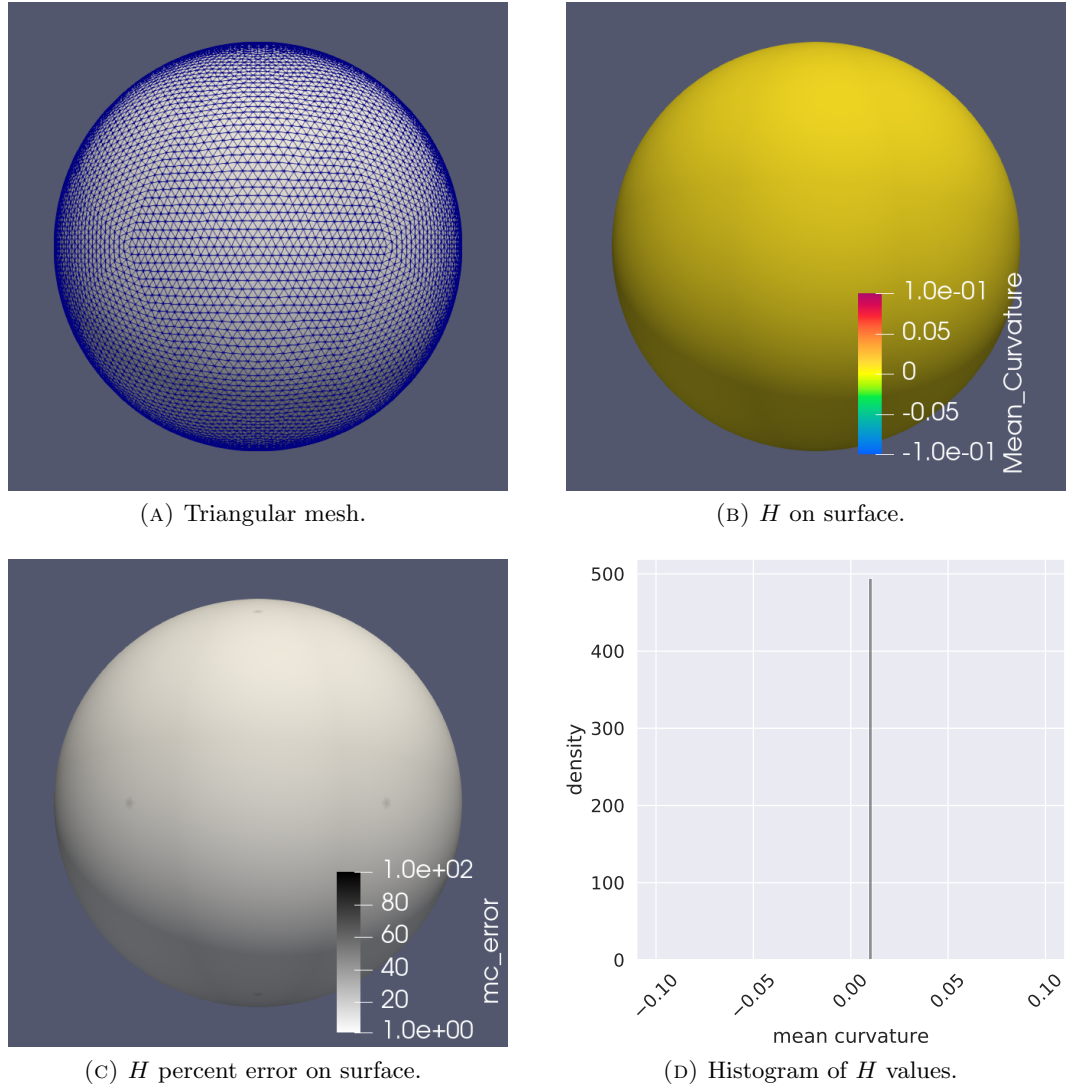


FIGURE 2.12: H for sphere mesh with $r = 100$. Mesh obtained by five subdivisions of icosahedron.

First, we decimate the otolith mesh by Meshlab’s Quadric Edge Collapse [46] filter. The decimation simplifies the mesh by reducing the number of vertices and faces and therefore reduces the presence of the closely spaced triangles that cause the ring-like artifacts. After the decimation is applied, the mesh is cleaned by removing unreferenced vertices and bad faces. Subsequently, we apply Taubin smoothing [47] to make the triangles in the mesh more equilateral. Taubin smoothing consists of two consecutive Laplacian smoothing [48] steps. The first step uses a positive scaling factor λ , and the second step uses a negative scaling factor μ with $\lambda > -\mu$, which prevents the volume from shrinking.

An overview of the transformations applied to improve the accuracy of H is demonstrated in Figure 2.13.

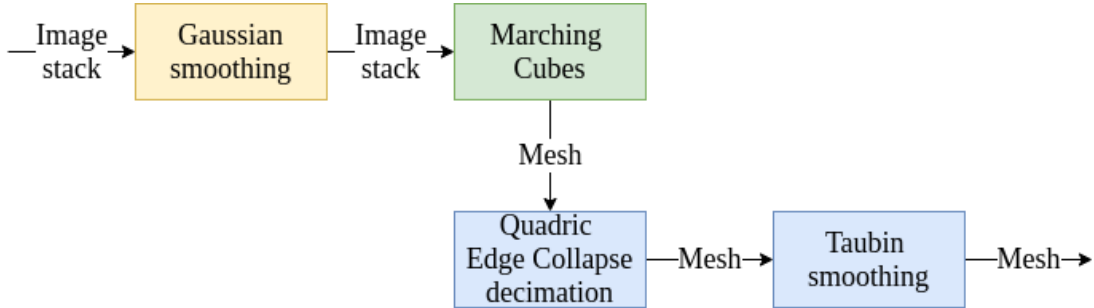


FIGURE 2.13: Transformations to improve accuracy of H for the otolith scans.

2.3.2.3 Assessment of the mesh improvements

In Figure 2.14 we assess the improvements of the above-described filters. The examined sphere mesh is generated by applying the filters to the Marching Cubes sphere mesh of Figure 2.11. It shows that the percent error of H is still excessive for some vertices (Figure 2.14c). The distribution plot (Figure 2.14d) shows the H values to be in the range of [0.0050, 0.0200]. The average H is 0.0110 with a standard deviation of 0.0040, which is a considerable improvement over the original mesh.

2.3.3 Detection of protuberances

To examine the protuberances, we develop a method to detect the protuberances in an otolith mesh. The method assumes that every protuberance contains one top, located on the otolith perimeter. Additionally, we note that some mature otoliths also contain protuberances which tops are located on the external face. Since it is hard to determine the exact dimensions of these structures, we ignore these types of protuberances.

Using the earlier established orientation of the otoliths, we remove the majority of vertices and edges of the otolith mesh that are not related to the tops of the protuberances. We achieve this by filtering the vertices and corresponding edges based on the properties of vertex p :

1. If p is positioned on a top, its normal vector points to either the xy -plane (see Figure 2.1a and Figure 2.1b) or the yz -plane (see Figure 2.1e and Figure 2.1f),
2. The tops of the protuberances are concave regions and therefore $H(p) > 0$.

In Figure 2.15 we demonstrate the resulting of filtering the vertices of an otolith meshes. As intended, we observe the filtrate to be mostly located on the otolith perimeter. However, some points are not located on the otolith perimeter, which we consider noise. We

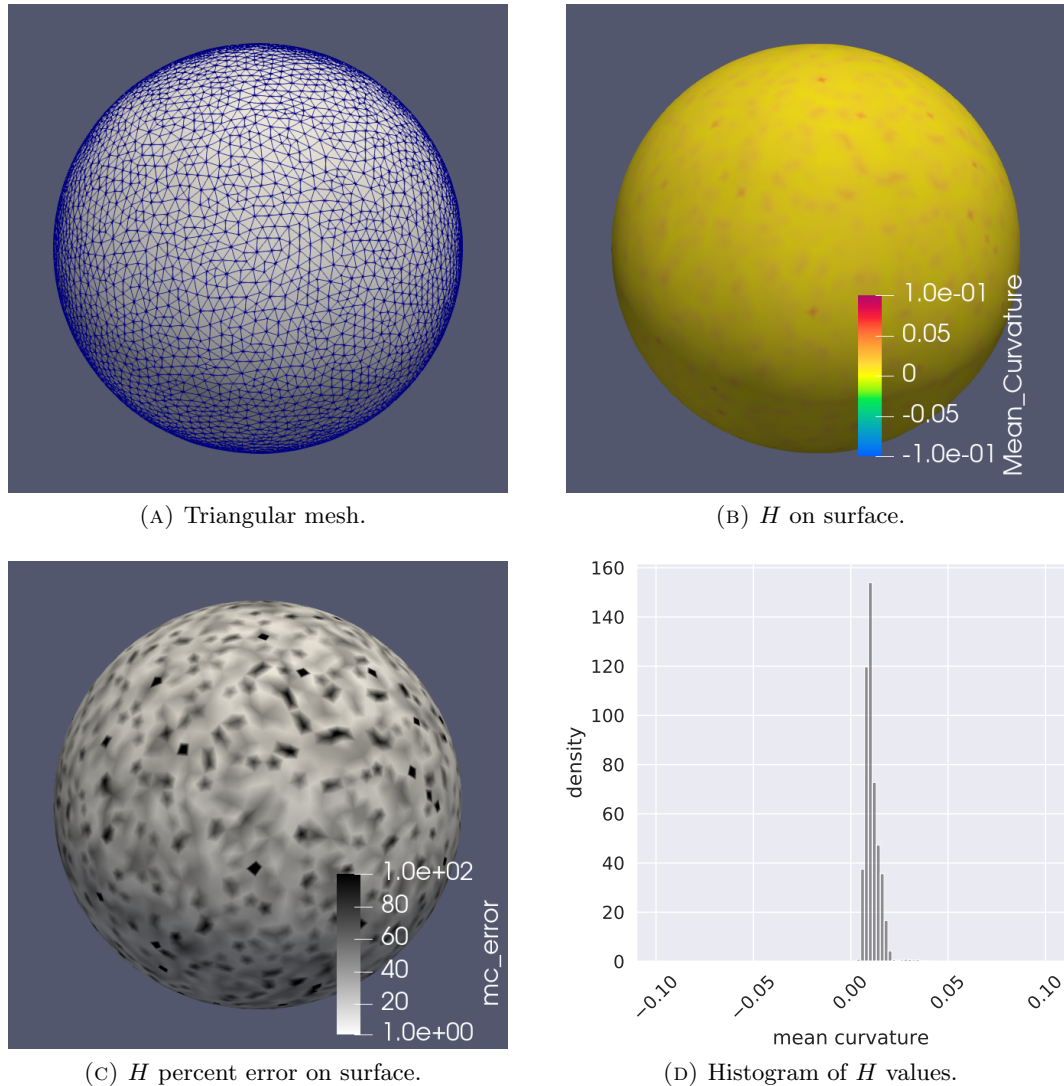


FIGURE 2.14: H of sphere with $r = 100$. Mesh generated by Marching Cubes, transformed through decimation and smoothing.

observe the noise for this particular otolith on the edge of the sulcus and the interruptions caused by the stitching process.

As a result of the filtering, we end up with several vertices and edges which together form connected components. Each component is labeled as being a single protuberance. Thereafter, we remove the components that do not meet a minimum amount of vertices N_{min} . Per otolith mesh, we manually determine N_{min} by analyzing the number of vertices in the smallest protuberances.

To eliminate the remaining noise clusters, we apply Density-based spatial clustering (DBSCAN) [49]. In DBSCAN, the euclidean distance parameter ϵ determines the maximum distance between two vertices to be considered neighbors. All vertices that are reachable through their neighbors are in one cluster. By setting a high ϵ , our objective

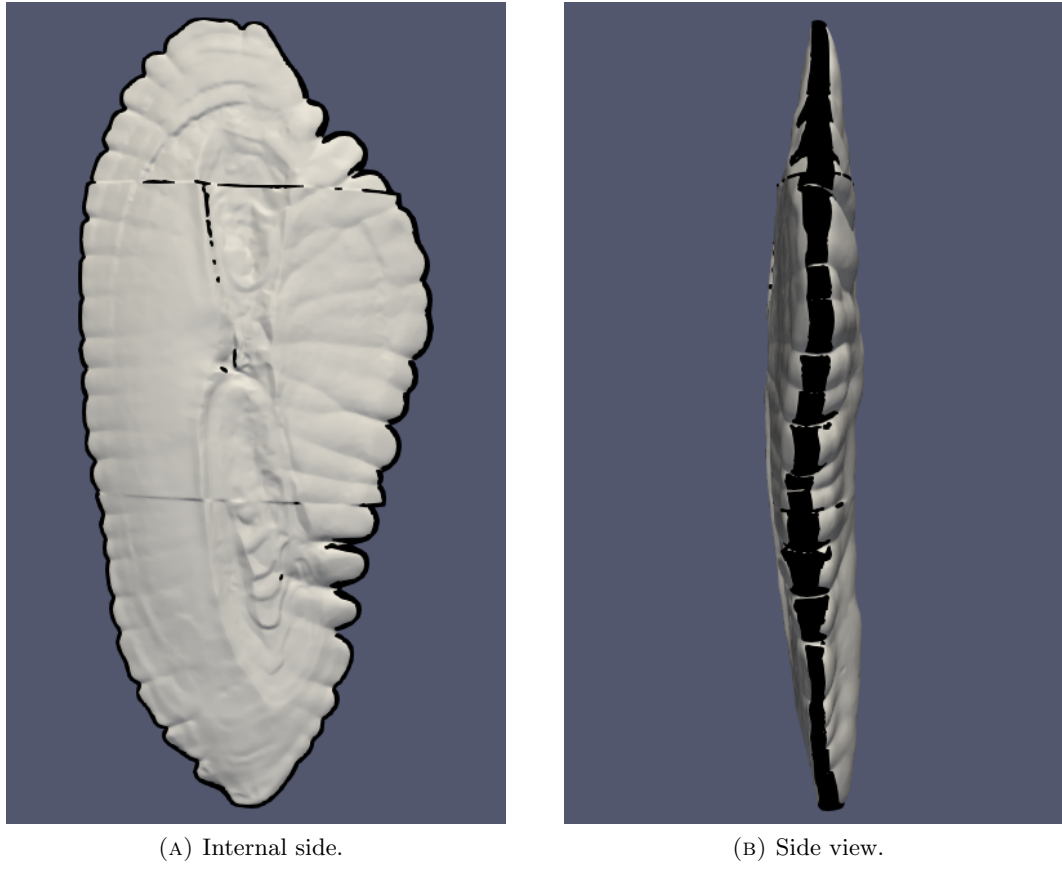


FIGURE 2.15: Components after filtering vertices on direction of the normal vector and value of H for otoI9.

is to group components that are located on the perimeter into one large cluster. Sequentially, this allows us to remove the remaining components located on the internal and external faces.

In Figure 2.16, we show the result of protuberance detection. We see that the regions on the sulcus and interruption are now discarded. Moreover, the different components are separated by color.

2.3.4 Experiments

After we derive H and successfully detect the protuberances, we perform several experiments to examine the otolith curvature.

2.3.4.1 Total length and protuberances

For our first experiment, we count the number of detected protuberances per otolith. Subsequently, we plot the total fish length against the number of detected protuberances

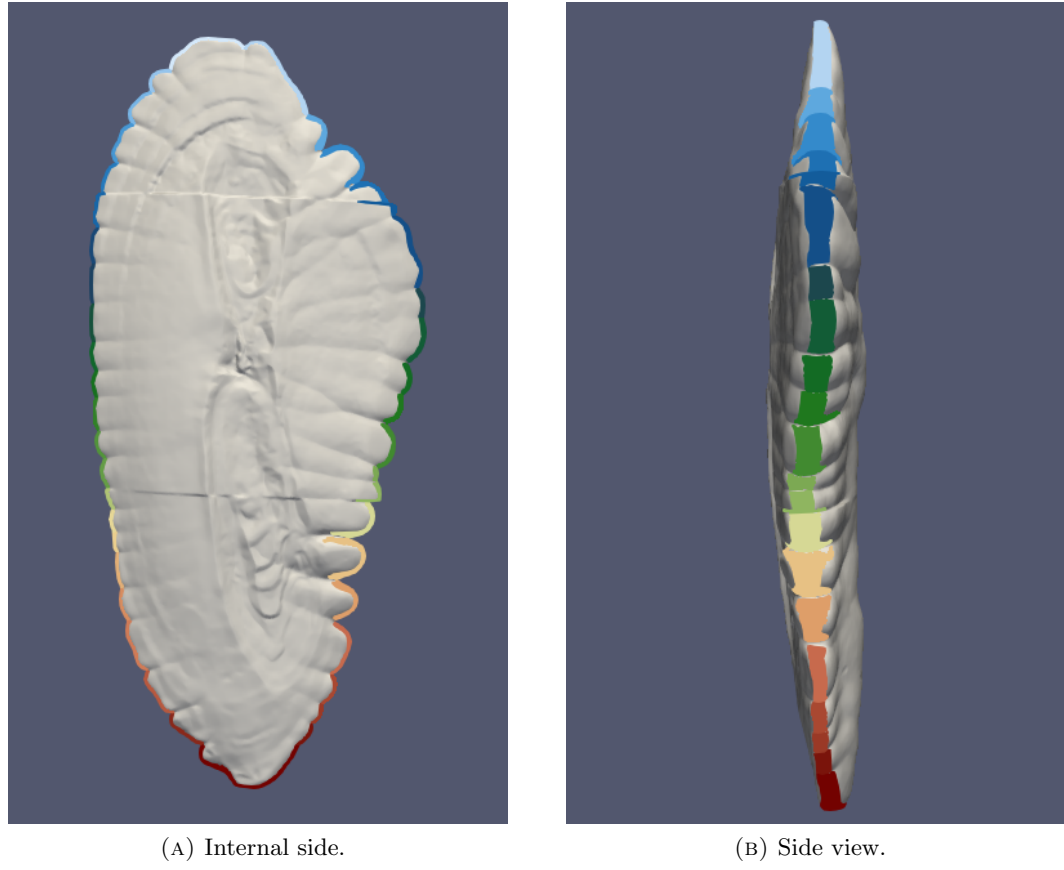


FIGURE 2.16: Detected protuberances for otoI9.

to examine a potential relationship. During this experiment, the total length only serves as an age indication. We separate the otoliths per gender which also provides an age indication. Additionally, gender separation also emphasizes potential sex dimorphism.

2.3.4.2 Mean curvature and gender

The female otoliths seem to contain more ridges and valleys in comparison to male otoliths of equal total length. To examine a potential sex dimorphism for the otolith curvature, we juxtapose the distributions of H for a female and male otolith of equal total length. This concerns the distribution of H on the entire otolith surface, including the internal and external faces of the otolith. In addition, we relate the distributions to the number of detected protuberances to find a potential correlation between the overall H and protuberances.

Chapter 3

Experiments and Results

In this chapter we present the results of the applied data transformations (section 3.1). Subsequently, we demonstrate the results of sulcus analysis (section 3.2) and the corresponding experiments (section 3.2.3). Finally, we show the results regarding the curvature analysis (section 3.3) and the curvature experiments (section 3.3.3).

3.1 Data transformation

We reduced the sizes of the otolith scans significantly through uniform resampling. Thereafter we apply rotation so that the otoliths align to the coordinate axes, and the proximal face is faced upwards.

To the scans of otoF75, otoM229, otoM278, otoM30, and otoM78, we applied an additional thresholding method to remove the non-empty background. Through the dilation technique, we tried to include the anti-alias voxels of the otoliths. However, these voxels are mostly mixed with background voxels making it difficult to find the boundaries. The background-removal method therefore inevitably reduced details of the otolith surface, as shown in Figure 3.1.

In Table 3.1, we show the dimensions of the image stacks after transforming, including magnification factor ω . The dimensions of the original image stacks are listed in Table 1.2.

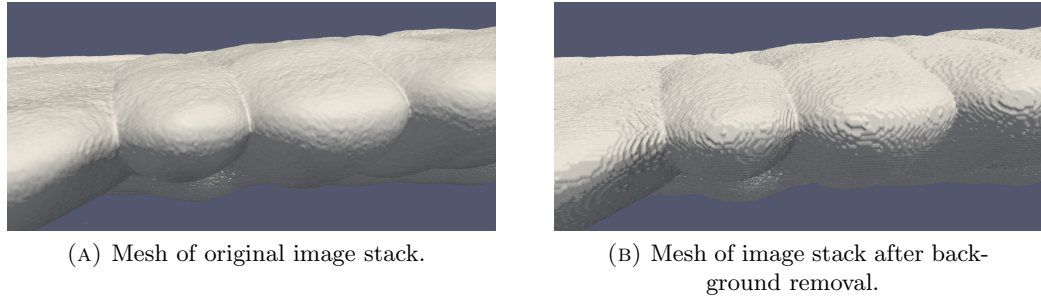


FIGURE 3.1: Surface reconstruction via Marching Cubes for otoM299.

TABLE 3.1: Dimensions of transformed otolith image stacks.

Label	Number of images	Image size (pixels)	ω
otoI48	1044	436×167	1
otoI47	2026	787×241	0.9
otoI96	1895	797×224	0.7
otoI59	1801	793×239	0.7
otoI89	1808	756×230	0.6
otoI9	1898	848×251	0.6
otoF75	1593	675×186	0.5
otoM30	1725	697×200	0.5
otoF176	1752	763×217	0.5
otoM78	1803	798×216	0.5
otoF200	1946	817×252	0.5
otoM145	1900	800×221	0.5
otoF11	1671	743×205	0.4
otoM203	1893	809×200	0.6
otoF34	1916	803×206	0.6
otoM19	1741	702×195	0.6
otoF198	1938	807×228	0.6
otoM150	1716	725×190	0.5
otoF83	1624	639×176	1
otoM229	1721	769×192	0.5
otoF73	1860	781×194	0.6
otoM278	1590	653×177	0.4
otoF177	1916	813×190	0.9
otoM257	1898	774×208	0.5

3.2 Analysis of the sulcus

3.2.1 Sulcus segmentation

During the sulcus segmentation process, we kept a consistent window length value of $m = 51$ to smooth E for all slices of the stacks. We used an increment of $l = 10$ for the peak detection loops, with the maximum distance between two slices to be considered neighbors $n = 10 \geq l$. As we applied interpolation to derive the sulcus peaks for

intermediate slices, this resulted in a smooth transition of the sulcus surface between consecutive slices. Finally, we manually adjusted a small amount of the automatically detected sulcus peaks to improve the accuracy of the corresponding segmentation.

In Figure 3.2, we visualize the obtained sulcus of a juvenile, female, and male saccular otolith.

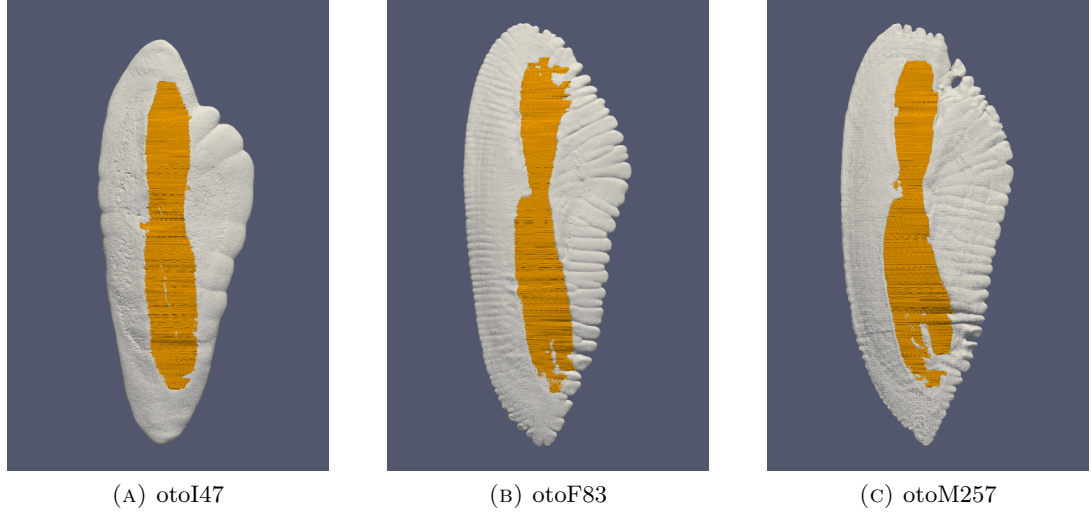


FIGURE 3.2: Proximal face of saccular otolith, including the obtained sulcus in orange.

3.2.2 Geometric measurements

In Table 3.2 we list the results of the surface area and volume estimations of the sulci and otoliths.

3.2.2.1 Comparison of volume estimates

Since the volume of the otoliths are estimated both digitally (Table 3.2) and manually (Table 1.1) we are able to make a comparison between the estimates, as shown in Table 3.3. We observe a relatively high average percentage difference (PD) of 14.40%. Once separated on gender, we notice the average PD for juveniles to be considerably higher (27.91%) in comparison to females (8.43%) and males (11.35%). We attribute this difference to the juvenile otoliths being significantly smaller in size, making them more prone to measurement inaccuracies regarding the manual volume estimation. Consequently, we used the digital volume estimates for the subsequent experiments.

TABLE 3.2: Computed surface area and volume estimates of the sulci and otoliths.

Label	Otolith surface area (mm ²)	Sulcus surface area (mm ²)	Otolith volume (mm ³)	Sulcus volume (mm ³)
otoI48	3.23	0.81	0.24	0.00
otoI47	12.72	3.66	1.60	0.05
otoI96	19.51	6.32	3.05	0.12
otoI59	18.91	5.43	3.10	0.09
otoI89	25.64	7.57	4.64	0.14
otoI9	30.12	7.95	5.71	0.12
otoF75	45.29	10.35	8.88	0.21
otoM30	45.42	10.70	9.59	0.19
otoF176	52.74	12.46	10.39	0.26
otoM78	58.06	11.10	11.18	0.22
otoF200	77.42	17.90	14.73	0.33
otoM145	58.35	15.60	11.75	0.40
otoF11	84.53	17.14	16.72	0.44
otoM203	87.03	21.11	18.10	0.63
otoF34	97.33	24.01	24.00	0.72
otoM19	78.89	22.78	19.81	0.68
otoF198	102.16	24.06	23.81	0.74
otoM150	95.65	23.94	23.79	0.66
otoF83	122.06	33.26	30.67	0.92
otoM229	109.33	26.59	31.40	1.07
otoF73	157.74	40.18	42.22	1.39
otoM278	146.70	29.64	48.43	1.27
otoF177	218.49	52.71	73.09	1.71
otoM257	215.21	57.11	78.80	3.05

3.2.3 Experiments

Using the acquired measurements, we perform experiments (section 2.2.4) to examine the relation between sulcus and otolith size. Since we express the size by both the surface area and the volume, the experiments are performed twice.

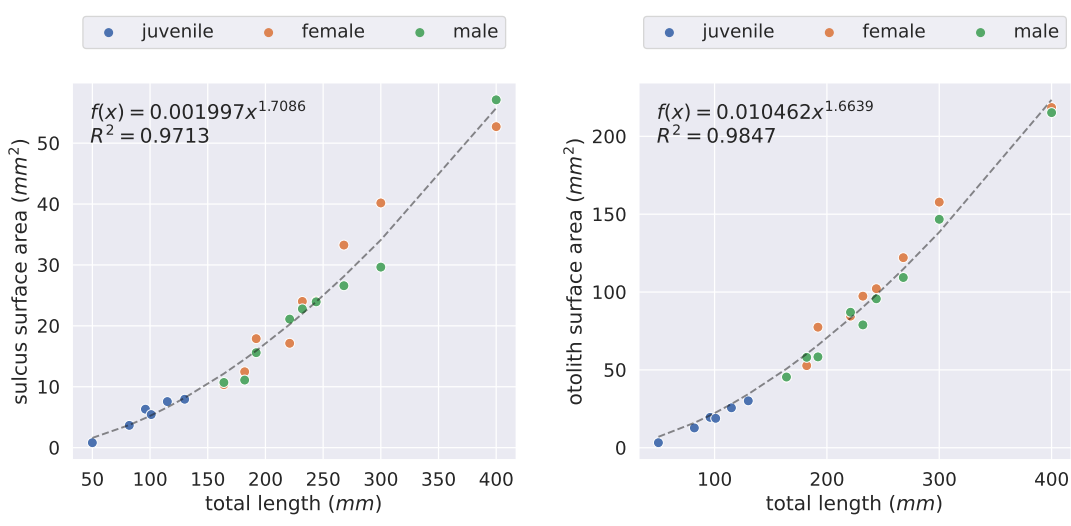
3.2.3.1 Surface area

In Figure 3.3, we examine the relationship between the total length (TL) of the individual, the sulcus surface area (SSA), and the otolith surface area (OSA). The fitted power equation ($R^2 = 0.97$) for the TL : SSA ratio (Figure 3.3a) shows us that there exists negative allometric growth between TL and the SSA. This also applies to the relationship between the TL and the OSA, which is also fitted by a power equation ($R^2 = 0.98$).

In Figure 3.4 we feature the experiments concerning the SSA : OSA ratio. We find a linear relationship between the SSA and OSA (Figure 3.4a).

TABLE 3.3: Comparison of digital and manual volume estimates of the otoliths.

Label	Otolith volume digital (mm^3)	Otolith volume manual (mm^3)	% Difference
otoI48	0.24	0.22	8.23
otoI47	1.60	1.13	35.58
otoI96	3.05	1.88	47.53
otoI59	3.10	2.22	33.15
otoI89	4.64	3.39	31.10
otoI9	5.71	5.07	11.86
otoF75	8.88	8.80	0.88
otoM30	9.59	10.16	5.79
otoF176	10.39	11.26	8.12
otoM78	11.18	12.99	14.98
otoF200	14.73	12.79	14.15
otoM145	11.75	14.74	22.58
otoF11	16.72	17.84	6.47
otoM203	18.10	20.55	12.67
otoF34	24.00	20.02	18.12
otoM19	19.81	23.05	15.09
otoF198	23.81	22.56	5.42
otoM150	23.79	25.96	8.71
otoF83	30.67	28.17	8.51
otoM229	31.40	32.40	3.13
otoF73	42.22	36.80	13.72
otoM278	48.43	42.28	13.56
otoF177	73.09	72.73	0.50
otoM257	78.80	83.39	5.66



(A) Total length vs. sulcus surface area. (B) Total length vs. otolith surface area.

FIGURE 3.3: Relationship between total length and surface area of sulcus and otolith.

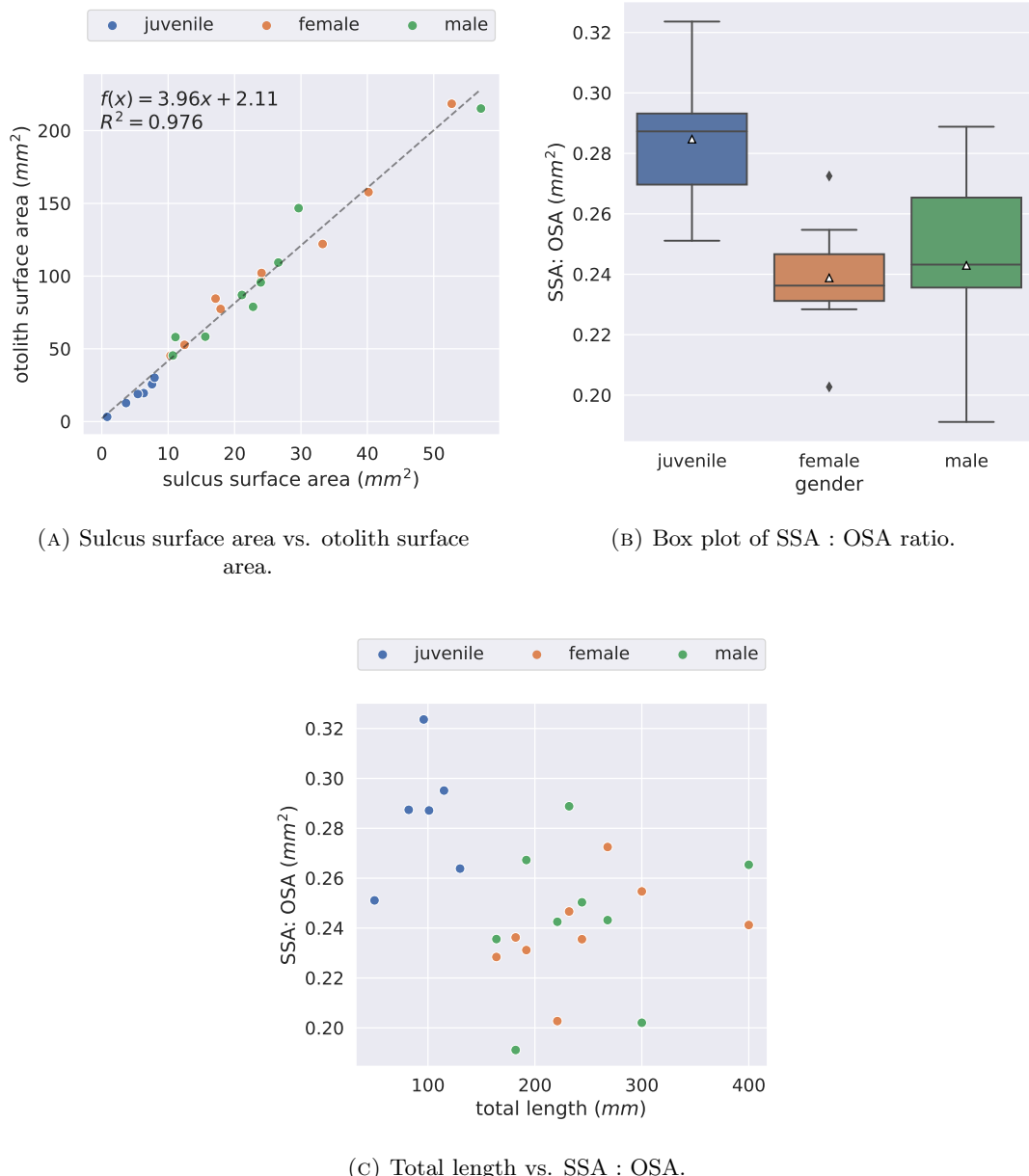
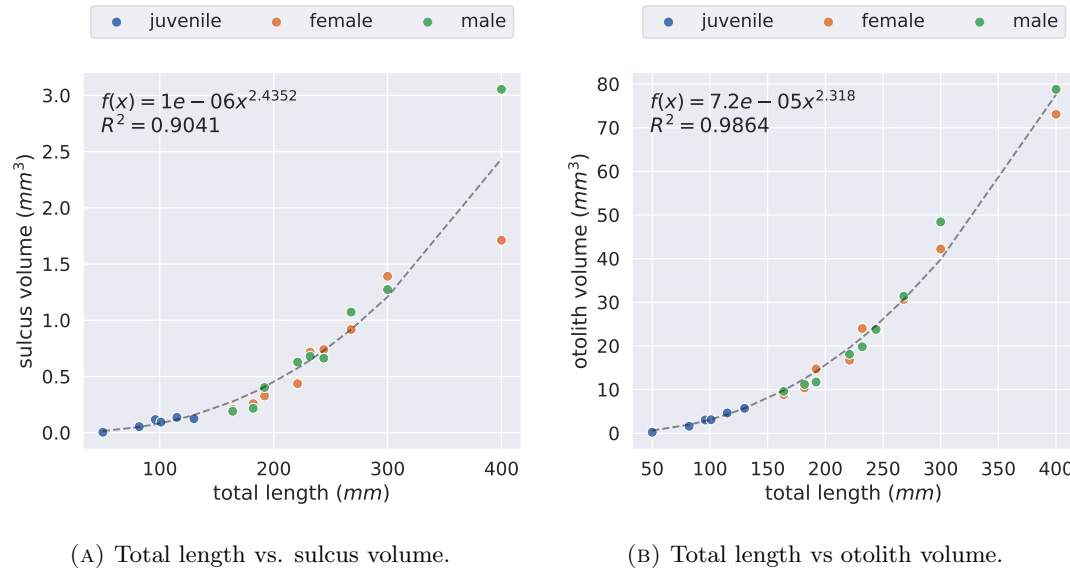


FIGURE 3.4: Experiments concerning the surface area of the sulci and otoliths of the European hake.

The box plot of Figure 3.4b demonstrates the distribution of the SSA : OSA ratio per gender. The average SSA : OSA ratio for all individuals is 0.2481. For juveniles, we find 0.2824, for females 0.2375, and for males 0.2392. This shows that mature hakes have a considerably lower average than the juveniles. Additionally, the average SSA : OSA ratio for males is higher compared to females.

In Figure 3.4c we plot the TL and the SSA : OSA ratio. As the values are too scattered, we are unable to fit an accurate equation to this relationship.



(A) Total length vs. sulcus volume. (B) Total length vs otolith volume.

FIGURE 3.5: Relationship between total length and volume of sulcus and otolith.

3.2.3.2 Volume

In Figure 3.5, we examine the relationship between the total length (TL), the sulcus volume (SV), and the otolith volume (OV). Between the TL and the SV, we fit a power equation by which we conclude a negative allometric relationship. Additionally, we observe the SV for the otoF177 and otoM257 (length 400 mm) to significantly deviate from the fitted equation, resulting in a lower $R^2 = 0.90$. For the OV of otoF177 and otoM257, the deviations are much smaller, and therefore the fitted power equation has a higher R^2 of 0.97. This power equation also demonstrates a negative allometric relationship, this time between the TL and the OV.

In Figure 3.6, we demonstrate the results of the experiments concerning the SV : OV ratio. Like the SSA : OSA ratio, the SV : OV ratio fits a linear equation (Figure 3.6a). For the SV : OV ratio, however, $R^2 = 0.93$ which is considerably lower.

We emphasize the differences of the SV : OV ratio per gender in the box plot of Figure 3.6b. The average SV : OV ratio for all individuals is 0.0274. For juveniles, this is 0.0273, for females 0.0265, and for males 0.0283. Again the ratio is higher for males. Additionally, we observe the ratio for females to be lower in comparison to juveniles.

Lastly, we plot the TL against the SV : OV ratio in Figure 3.6c. Also for this plot, the values are too scattered to fit an equation.

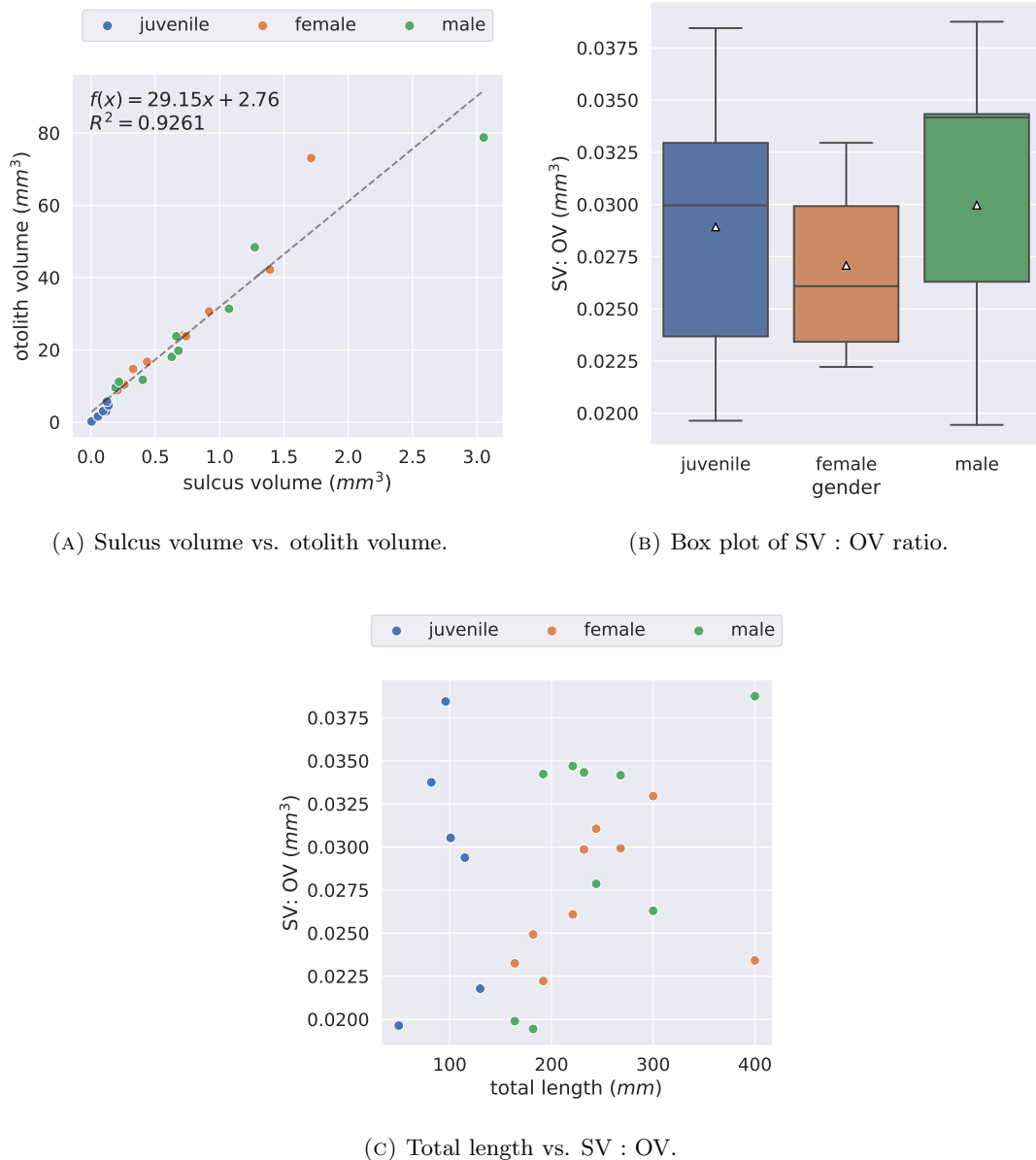


FIGURE 3.6: Experiments concerning the volume of the sulci and otoliths of the European hake.

3.3 Analysis of the curvature

3.3.1 Preparing the otolith scans

To improve the continuity of the distribution of H on the otolith meshes, we applied additional transformations to the digital otoliths (Figure 2.13). First, we smoothed the corresponding image stacks through 3D Gaussian smoothing with $\sigma = 3$. This reduced the observed grain texture while largely preserving the natural boundaries of the otoliths. Additionally, it reduced the presence of the interruptions caused by the stitching process

and smoothed the discontinuous surfaces provoked by the background removal (Figure 2.2). Subsequently, we generated Marching Cubes meshes of the smoothed stacks. We then applied Quadric Edge Collapse decimation to the meshes, with the reduction set to 50%. We apply this filter four times so that the resulting mesh has $\frac{1}{2}^4$ the number of triangles of the original mesh.

While this seems like a large reduction, the original otolith meshes consist of millions of triangles and therefore possess an unnecessary amount of detail, including the mentioned ring-like artifacts. The applied triangle reduction of $\frac{1}{2}^4$ proved to be sufficient to reduce these artifacts while largely preserving the original boundaries of the otolith meshes.

Finally, we applied 40 iterations of Taubin smoothing with $\lambda = 0.5$ and $\mu = -0.53$. For a larger number of iterations, the improvement of the equilateral property of the triangles stagnated.

In Figure 3.7, we visually compare the distribution of H for an original Marching Cubes mesh and a transformed mesh. The figure demonstrates the effects of decimation and Taubin smoothing on the continuity of H on the otolith surface.

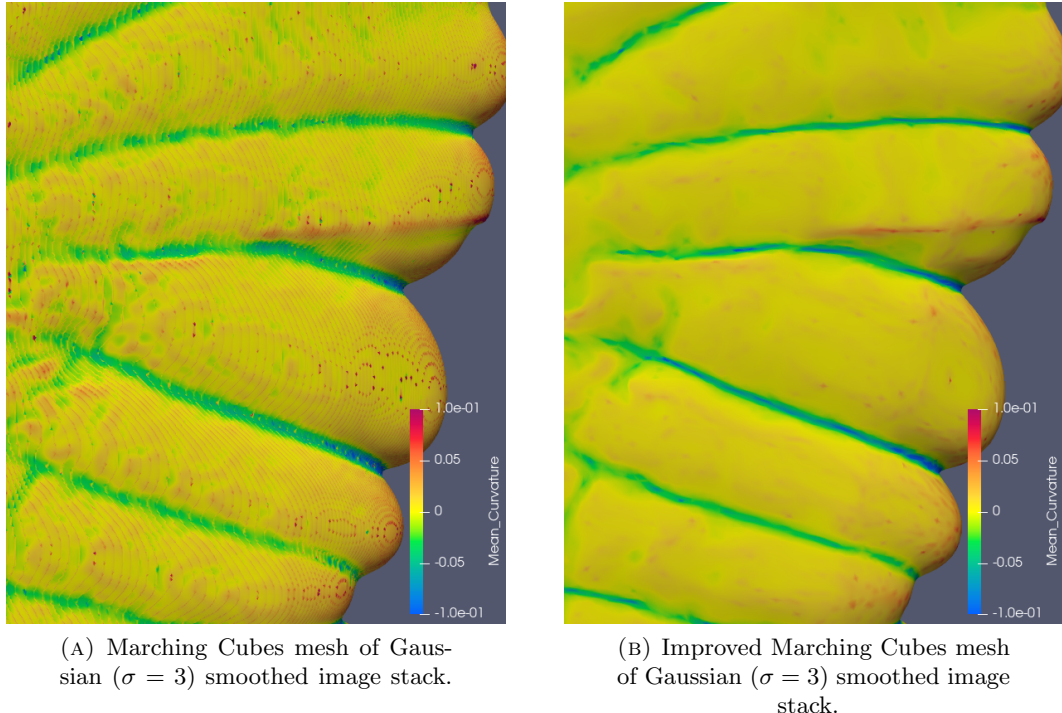
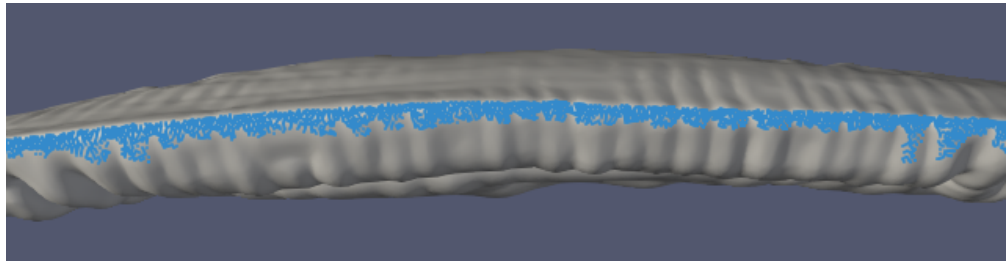


FIGURE 3.7: H on mesh of otoF73.

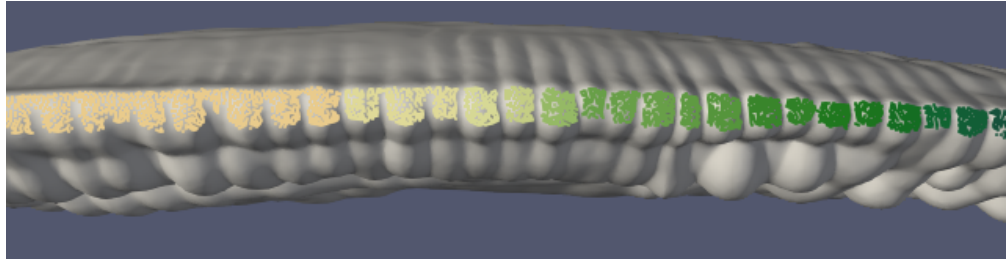
3.3.2 Detection of protuberances

Through the application of the protuberance detection method to the otoliths, we make multiple observations. First, we notice that most otoliths possess a specific region on the otolith perimeter that contains a considerable amount of closely spaced protuberances. In Figure 3.8, we visualize the concerning region for two female otoliths. For otoF83 (Figure 3.8a), our method detects the specific region to contain one large elongated protuberance. Alternatively, it detects multiple smaller protuberances in the same region for otoF73 (Figure 3.8b). For the latter otolith, the protuberances are more pronounced as they are surrounded by valleys, characterized by regions where $H < 0$. Consequently, we detected a total of 43 protuberances for otoF83 and 73 protuberances for otoF73, while the difference in total length is only 32 mm. In the subsequent sections, we refer to this region on the otolith perimeter as the elongated region.

Typically, we find a $10 < N_{min} < 50$.



(A) otoF83 (268 mm)



(B) otoF73 (300 mm).

FIGURE 3.8: Detected protuberances (separated by color) on the elongated region of the otoliths.

Another observation regards the clustering through DBSCAN, as described in section 2.3.3. Its objective is to exclude components that were not located on the otolith perimeter. Regarding the internal face of the otolith, the clustering achieved the intended effect. For the external face, however, the clustering method turned out to be insufficient. Some noise components are relatively close to the otolith perimeter and therefore are not excluded. Eventually, we removed these components manually.

3.3.3 Experiments

3.3.3.1 Protuberances and total length

To elaborate on the difference in protuberances for juvenile and mature otoliths, we plot the TL against the number of detected protuberances (Figure 3.9). The figure shows that for juvenile otoliths, the number of protuberances increases as the fish grows. For mature otoliths, the variability in the number of protuberances is too significant. Correspondingly, we do not observe a growth for mature otoliths.

Moreover, the plot shows us that between females and males of equal TL, the number of detected otolith protuberances is consistently higher for females. This excludes the pair of length 182 mm, where the male has 4 more detected protuberances, and the pair of length 164 mm, which have an equal amount. Finally, we observe that the otoliths of some of the longest fish have a lower amount of detected protuberances than some of the juvenile otoliths.

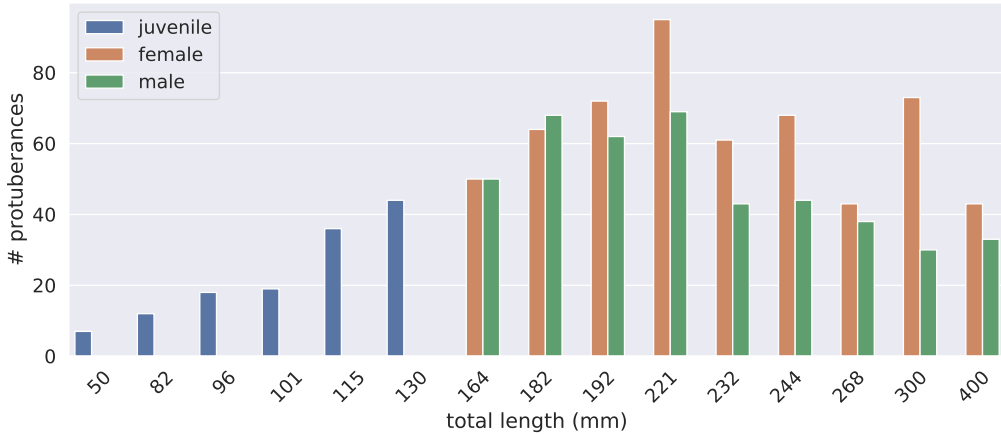


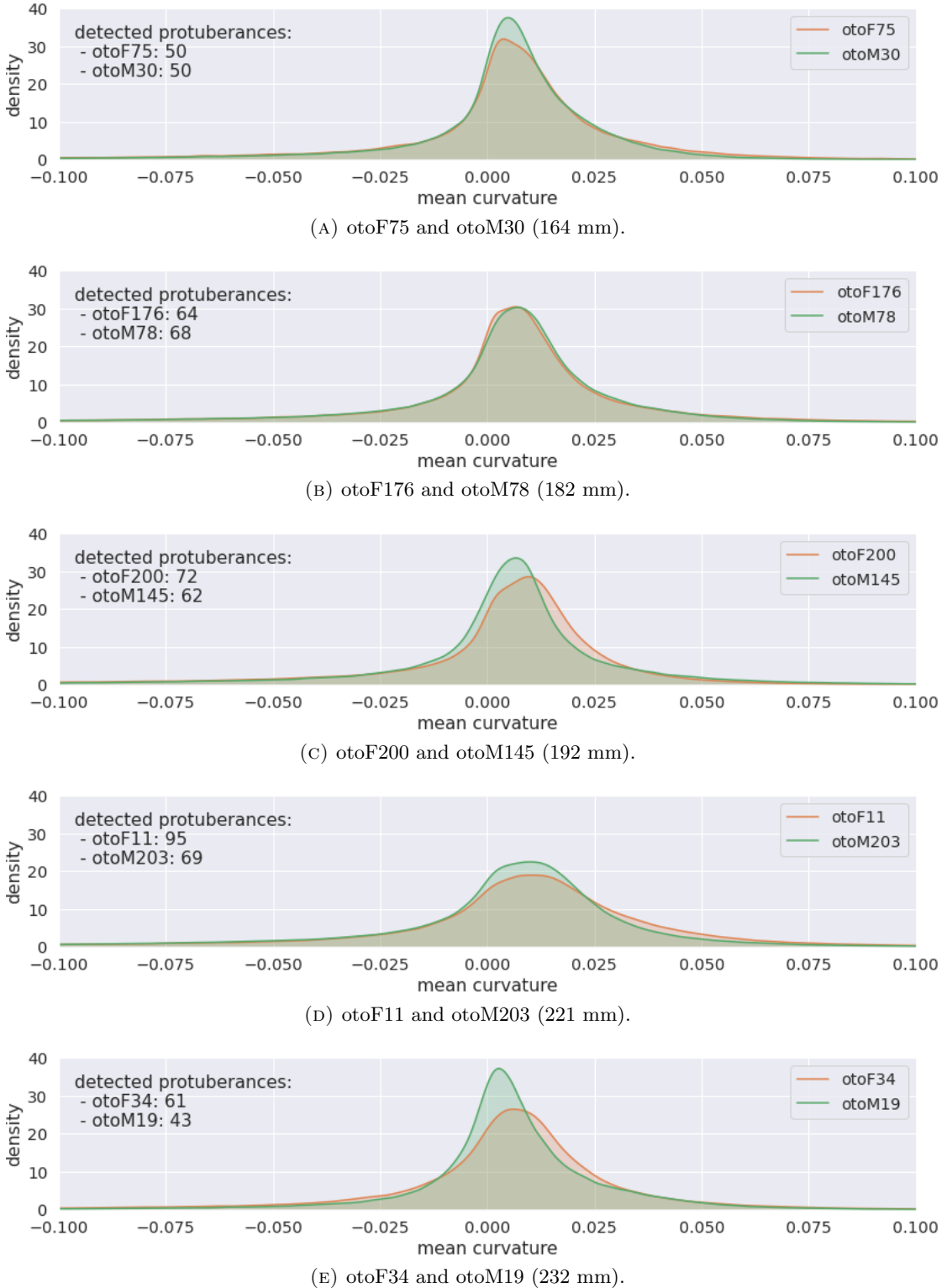
FIGURE 3.9: Number of detected protuberances per TL.

3.3.3.2 Mean curvature and gender

To emphasize a potential sex dimorphism, we compare the distribution of H for female and male otoliths of equal total length. In addition, we take the number of detected protuberances per otolith into account.

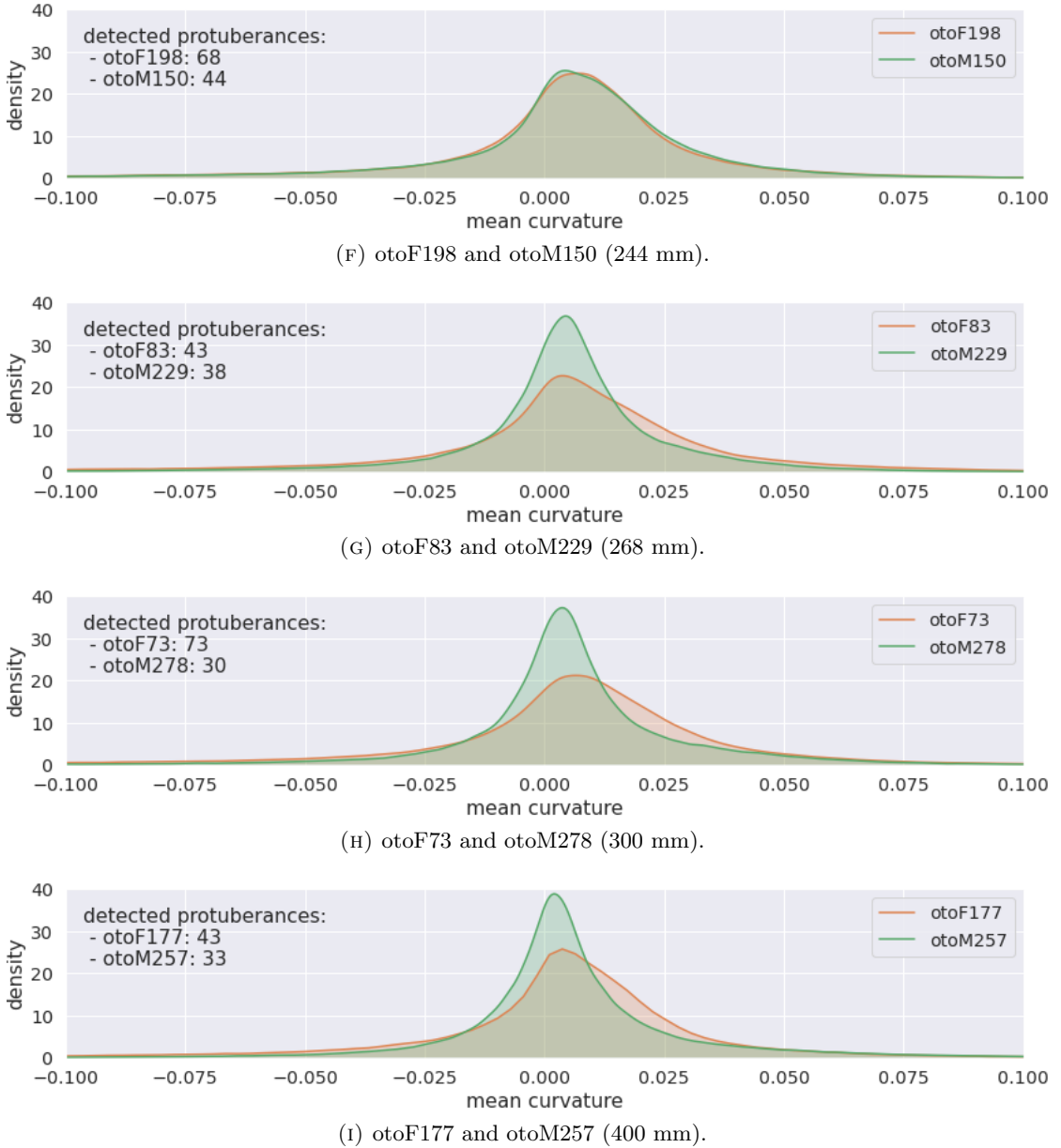
The result of the experiment is shown in Figure 3.10, where we visualize the distributions by through the kernel density estimations (KDE). Per pair, we make several observations:

- (A) The pair of 164 mm (Figure 3.10a) is the only pair where both otoliths have an equal number of detected protuberances. We do, however, observe a small



difference between the density curves. A visual comparison between the otolith surfaces shows that for both otoliths, the elongated region is pronounced.

- (B) As mentioned earlier, the pair of 182 mm (Figure 3.10b) is the only pair where the number of detected protuberances is higher for the male. The observed difference

FIGURE 3.10: KDE plots for H on surface of male-female pairs.

in the density curves is minimal. Again, for both otoliths, the elongated region is pronounced.

- (C) The density curve for otoF200 (Figure 3.10c) contains considerably more positive H values in comparison to otoM145. This is reflected by the difference in the number of detected protuberance which is 10. Also for this pair, the elongated region is pronounced for both otoliths.
- (D) The difference in the number of detected protuberances is 26 for the pair of length 221 mm (Figure 3.10d). This is a big difference, while the density curves do not

show a big difference. We can see that for both otoliths, the elongated region is pronounced.

- (E) The density curves in Figure 3.10e differ evidently. A visual comparison between the otolith meshes shows us that, expectantly, the protuberances of otoF34 are more pronounced. Alternatively, the elongated region for otoM19 is exceptionally smooth, which explains the difference in the number of detected protuberances to be 18.
- (F) Just like the pair of length 182 mm, the density curves for the pair of length 244 mm (Figure 3.10f) are almost identical. This is not reflected by the number of the detected protuberance, which shows a considerable difference of 24. We notice the elongated region of otoF198 to contain tens of protuberances while otoM150 possesses a maximum of three protuberances in this region.
- (G) The density curves of the pair of length 268 mm (Figure 3.10g) show a significant difference, though the difference in detected protuberances is small. We attribute this contradiction to the external face of otoF83 being pronounced in contrast to otoM299. Both otoliths show an underdeveloped elongated region, explaining the relatively small number of overall detected protuberances.
- (H) The biggest difference in the number of protuberances is 42, observed for the pair of 300 mm (Figure 3.10h). The density curves demonstrate that the H distributions are also significantly different. When we visualize the otolith meshes, we notice otoM278 being remarkably smooth, especially on its external face.
- (I) For the pair of length 400 mm (Figure 3.10i), the difference in the number of detected protuberances is 10. The corresponding density curves show a significant difference. A visual comparison of the otolith surfaces demonstrates that the elongated region for both otoliths is not pronounced. This could explain the relatively low numbers of detected protuberances. In addition, the elongated region of otoM257 seems to be completely eroded (see Figure 1.4f).

The peaks of the density curves for H of male otoliths are consistently higher than their female counterparts. This is emphasized by Figure 3.11, where we visualize the density curves for H of all female and male otoliths combined. Consequently, the H values on male otoliths are more uniform which indicates a more smooth surface. In addition, the plot shows us that the average number of detected protuberances for females is higher in comparison to male otoliths.

Finally, we observe that a significant difference in the number of the detected protuberance does not imply a significant difference between the corresponding density curves.

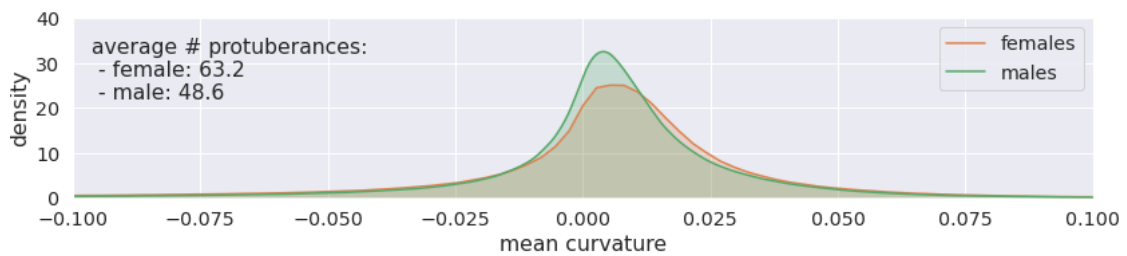


FIGURE 3.11: KDE plots for H on surface of all female and male otoliths.

Chapter 4

Discussion

In this chapter, we discuss the limitations encountered during the execution of our methods and the corresponding experiments. Thereafter, we interpret the results of the experiments.

4.1 Analysis of the sulcus

4.1.1 Segmentation of the sulcus

The shape of the sulcus is largely unclear in slices at the start and end of an image stack. Sequentially, the detection of peaks is complicated. Moreover, when the algorithm is able to detect peaks in such slices, it is difficult to manually determine whether the peaks are related to the sulcus or should be considered noise.

In addition, we are unable to algorithmically assess the quality of the acquired sulcus due to the ill-defined boundaries of the sulcus and the associated groove. To obtain a naturally shaped sulcus, we visually analyzed whether the acquired sulcus peaks yielded a desirable result. If this was not the case, we adjusted the causing peaks. We note this introduces a bias, potentially giving incorrect results.

4.1.2 Geometric measurements

The acquired sulcus image stacks consist of 2D binary images. Consequently, Marching Cubes is unable to apply interpolation to the edges resulting in discrete surfaces for the sulcus meshes. This possibly affects the corresponding geometric measurements.

Furthermore, the error observed during the geometric measurements of the sphere meshes (2.8) transfers to the measurements of the sulcus and otolith meshes. Since the observed errors for the spheres are almost negligible, we assume the error for the sulci and otoliths to also be insignificant. However, the sulcus and otolith meshes contain an additional error that is caused by the resampling of the otolith image stacks.

Lastly, we examined alternative methods to estimate the measurements of the sulci and otoliths. Here, the surface area can be estimated by counting the voxels on the circumference of the object in the image stack, without the interference of Marching Cubes. Likewise, the volume can be estimated by directly counting the voxels in the image stack. These methods yielded higher errors for the spheres (Figure 2.8) in comparison to the methods discussed in section 2.2.2. We attribute this to the mesh representations being more accurate representations since they are not bounded to the voxel grid. This is the result of the interpolation applied by Marching Cubes on the edges, which considers the anti-alias voxels. Alternatively, when the surface area or volume is obtained by counting the voxels, it is difficult to determine which voxels should be considered.

4.1.3 Experiments

4.1.3.1 Surface area

We replicated the experiments of Lombarte [20], who examine the S : O ratio through the proximal surface area, for the *M. capensis* and *M. paradoxus*. During our research, we examined the S : O ratio through the entire surface area of the saccular otolith of European hakes, *M. merluccius*. Despite discrepancies in species and the expression of the surface area, we expect to find similar relations as the hake is of the same genus as the *M. capensis* and *M. paradoxus*. Moreover, we assume the proximal surface of the otolith to be a constant portion of the total otolith surface area.

Both the TL : SSA ratio (Figure 3.3a) and the TL : OSA ratio (Figure 3.3b) fit a power equation. However, the slope of the equation of the former is significantly lower. Accordingly, the average SSA : OSA ratio for longer hakes is lower. Additionally, we observe that the average SSA : OSA ratio for mature hakes is lower compared to juvenile hakes (Figure 3.4b). This is following our assumption that juvenile hakes have larger S : O ratios as they inhabit deeper sea levels, thus are more dependent on hearing abilities.

However, the protuberances most likely have a significant influence on the SSA : OSA ratio, as their presence influences the OSA measurements while barely affecting the SSA measurements. We assume that a higher presence of pronounced protuberances, as observed for mature hakes, contributes to a lower SSA : OSA ratio. Consequently, our assumption

that the otolith proximal surface area is a constant portion of the otolith surface area seems incorrect. To reduce the influence of the protuberances on the ratio, it would be more suitable to examine the size of the sulcus and otolith through their proximal surface area. Unlike the SSA : OSA ratio, the proximal surface areas are barely influenced by the presence of the protuberances.

Subsequently, we expect negative allometric growth between the TL and the SSA : OSA ratio. However, we cannot confirm this assumption as we are unable to fit an equation to the TL and the SSA : OSA ratio. A larger sample size could allow us to fit an equation with a high R^2 . The relatively small sample size limits us anyway as a larger sample size would also improve the quality of the results of the other experiments. However, we note that digital 3D representations of otoliths are rare and costly to obtain.

4.1.3.2 Volume

Regarding the TL, the SV of otoF177 is significantly below average, whereas the SV of otoM257 is significantly above average (Figure 3.5a). Since the corresponding OV (Figure 3.5b) do not show such deviations, the SV : OV ratio has considerable deviations for otoF177 and otoM257 (Figure 3.6a). Consequently, R^2 for the SV : OV ratio is lower compared to R^2 for the SSA : OSA ratio. However, due to the small sample size, this observation can be ascribed to a coincidence.

Additionally, the difference between the slope of the TL : SV ratio and the TL : OV ratio is less significant compared to the surface area substitutes. Correspondingly, the SV : OV ratio (Figure 3.6b) is more evenly distributed per gender than the SSA : OSA ratio.

As stated previously, we assume that a higher presence of protuberances contributes to a lower SSA : OSA ratio. The impact of the protuberances on the OV is presumably less significant and thus the SV : OV ratio is less affected. Accordingly, the distributions of the SV : OV ratio for juvenile, male, and female hakes are more similar. Once more, a larger sample size could provide a definite answer as this could confirm or disprove a constant relation between the TL and the SV : OV ratio (Figure 3.6c).

4.2 Analysis of the curvature

4.2.1 Mean curvature derivation

Many papers discuss the difficulties regarding the curvature derivation for digital volumes. Since most of the presented solutions are not easily accessible nor implementable, we were limited to the use of free and open-source software such as VTK, Marching Cubes, ParaView, and Meshlab.

Nevertheless, we are able to improve H for the sphere mesh (Figure 2.14). The improved sphere mesh does, however, still contain a significant error for H . Since the improved otolith meshes are generated following the same procedure, we expect them to contain a similar error. As we do not know the ground truth for H on the otolith meshes, the exact error is indeterminable.

Subsequently, we note that the applied Gaussian smoothing reduced the grain-texture. The derived H values therefore mostly relate to the edges of the protuberances and the sulcus.

4.2.2 Detection of the protuberances

Our protuberance detection method is based on the assumption that every protuberance has a distinct top on the otolith perimeter, that is surrounded by a convex surface. In other words, we identify a protuberance merely by its top. While this seems sufficient to algorithmically derive the number of protuberances it introduces some limitations.

A protuberance may be very clear-cut but as long as the associated top is not, our detection method is unable to identify it as being an individual protuberance. This mostly applies to tops on the elongated region. The distinctiveness of tops in this region does not seem to be related to the TL. We observed smooth elongated regions for mature otoliths of longer fish (otoF83, otoM299, otoM278, and otoM257) whereas the external faces are wrinkled. Contrary, we observed distinct elongated regions for some shorter mature otoliths (otoF75, otoM30, otoF176, and otoM278).

Finally, we recall that a fraction of the protuberances has a top on the external face of the otolith. Since we are unable to make an algorithmic distinction between such tops and noise regions on the external face, we remove these tops, which introduces a bias.

4.2.3 Experiments

4.2.3.1 Total length and protuberances

Some longer hakes have fewer detected protuberances in comparison to shorter or juvenile individuals. This variability is largely the result of the discussed inabilitys of our method. Additionally, it is partly due to the otolith morphology, which shows that the otoliths of some longer hakes simply have fewer protuberances.

From this, we conclude that the tops of the protuberances do not provide enough information to examine the formation of the protuberances relative to the TL. Perhaps, other characteristics are more relevant for this experiment, such as the local mean curvature or the protuberance length. Due to a lack of time, we were unable to explore these options.

4.2.3.2 Mean curvature and gender

As mentioned earlier, there is an indeterminable error for H on the otolith meshes. The error is most likely the result of the multiple discretization processes that take place to transform the actual otoliths into triangular meshes. Furthermore, we assume the error to be similar for otolith meshes that originate from fishes of equal TL as they have a comparable topology. This allowed us to make a comparison between the corresponding density curves (Figure 3.10).

During the experiments, we observe that a significant difference in the density curves of H does not imply a significant difference in the number of detected protuberances. We explain this by the fact that over time the existing protuberances become more distinct which influences the H density curves. However, after a certain threshold, the distinctiveness of the protuberance shape does not influence the number of detected protuberances. Overall, the density curves possibly provide a better idea of the formation of the protuberances.

Chapter 5

Conclusion and Future Work

5.1 Analysis of the sulcus

The otolith scans are used to segment the sulcus according to a developed method. This allows the estimation of the surface area and volume of the sulcus. Subsequently, experiments are performed concerning the estimates to find an answer to the research question:

RQ 1: How does the saccular sulcus size relate to the saccular otolith size for the European hake?

During this research, the size of the sulcus and otolith is expressed through the surface area and volume. Consequently, the answer to the research question is two-fold:

- The relationship between the sulcus surface area (SSA) and the saccular otolith surface area (OSA) is linear for the European hake. The SSA growth with respect to the total length is negative allometric. This also applies to the OSA growth with respect to the total length. The slope for the latter relation is higher than the former resulting in a lower SSA : OSA ratio for longer hakes. This is following our assumption that the SSA : OSA ratio is higher for juvenile hakes which typically inhabit the sea at deeper levels and therefore are more dependent on their hearing. However, a higher presence of protuberances, as observed for mature hakes, presumably contributes to a lower SSA : OSA ratio. Since the proximal surface barely contains any protuberances, it would be more appropriate to examine the proximal surface area of the sulcus and the otolith to reduce the influence of the protuberances on the ratio.

- For the European hake, the relationship between the sulcus volume (SV) and the saccular otolith volume (OV) is linear. The SV growth relative to the total length is negative allometric. Likewise, the OV growth with respect to the total length is negative allometric. The difference between the slopes for both relationships is less significant in comparison to the surface area alternatives. Consequently, the SV : OV ratios per gender are more evenly distributed in comparison to the SSA : OSA ratio. This implies that the effect of the protuberances on the SV : OV ratio is less significant compared to the SSA : OSA ratio.

5.2 Analysis of the curvature

To analyze the curvature of the saccular otoliths, the mean curvature H on the otolith surface is derived. Despite several applied improvements, the acquired H values contain a significant but indeterminable error.

The presence of protuberances has a strong influence on the H values. Therefore, to elaborate on the curvature, a method is developed to detect the protuberances in the otolith scans. The method is based on the localization of the tops of the protuberances on the otolith perimeter. Subsequently, experiments are performed on the curvature and the protuberances for the saccular otoliths to answer the research question:

RQ 2: How does the curvature of the saccular otolith of the European hake change over time?

For the juvenile otoliths, the number of detected protuberances increases as the total length increase. Due to high variability in the number of detected protuberances, this growth is not observed for mature hakes. Alternatively, some otoliths of the longest fish have fewer detected protuberances compared to some juvenile otoliths. Moreover, a sex dimorphism is observed as the number of detected protuberances is higher for female otolith than for male otoliths of equal total length.

Following the sex dimorphism, the peaks of the H density curves for saccular otoliths are also higher for females compared to male otoliths. Consequently, the H values on the male otoliths are more uniform, which indicates a smoother surface.

5.3 Future work

5.3.1 Analysis of the sulcus

First and foremost, future research regarding the S : O ratio of the European hake should focus on the extraction of the proximal surface of the sulci and otoliths. This allows quantifying the influence of the protuberances on the SSA : OSA ratio, which could either confirm or disprove our statement.

Finally, the 3D representations of the sulci and otoliths allow the derivation of several other 3D geometric measurements that can be studied.

5.3.2 Analysis of the curvature

As the curvature analysis concerns, future research should focus on the implementation of the solutions presented in the literature to improve the accuracy of H for the otolith scans. Possibilities include the use of different surface reconstruction algorithms such as Marching Tetrahedra, Dual Marching Cubes, or SurfaceNets. Additionally, H could be derived directly from the voxels of the otolith scans without the interference of meshes.

The protuberance detection method offers room for improvement. Here, possibilities should be examined to extract the entire protuberance instead of merely its top. This possibly provides a more clear picture of the protuberance growth since this would allow obtaining additional characteristics, such as the protuberance length and width.

Bibliography

- [1] Jürgen Alheit and T Pitcher. *Hake fisheries, ecology and markets*. Chapman & Hall, 1995.
- [2] W Fisher, ML Bauchot, and M Schneider. Fiches fao d'identification des espèces pour les besoins de la pêche (révision 1). *Méditerranée et mer Noire, zone de pêche*, 37, 1987.
- [3] Valerio Bartolino, Alessandro Ottavi, Francesco Colloca, Gian Domenico Ardizzone, and Gunnar Stefánsson. Bathymetric preferences of juvenile european hake (*merluccius merluccius*). *ICES Journal of Marine Science*, 65(6):963–969, 2008.
- [4] Virginia Carrozzi, Manfredi Di Lorenzo, Daniela Massi, Antonino Titone, Giandomenico Ardizzone, and Francesco Colloca. Prey preferences and ontogenetic diet shift of european hake *merluccius merluccius* (linnaeus, 1758) in the central mediterraneanásea. *Regional Studies in Marine Science*, 25:100440, 2019.
- [5] Arie Schuijf. Models of acoustic localization. In *Hearing and sound communication in fishes*, pages 267–310. Springer, 1981.
- [6] Beatriz Morales-Nin. Review of the growth regulation processes of otolith daily increment formation. *Fisheries Research*, 46(1-3):53–67, 2000.
- [7] Steven E Campana. Chemistry and composition of fish otoliths: pathways, mechanisms and applications. *Marine Ecology Progress Series*, 188:263–297, 1999.
- [8] Steven E Campana and John D Neilson. Microstructure of fish otoliths. *Canadian Journal of Fisheries and Aquatic Sciences*, 42(5):1014–1032, 1985.
- [9] Tanja Schulz-Mirbach, Martin Heß, and Martin Plath. Inner ear morphology in the atlantic molly *poecilia mexicana*—first detailed microanatomical study of the inner ear of a cyprinodontiform species. *PLoS One*, 6(11):e27734, 2011.
- [10] Arthur N Popper and Richard R Fay. Sound detection and processing by fish: critical review and major research questions (part 1 of 2). *Brain, behavior and evolution*, 41(1):14–25, 1993.

- [11] Victor M Tuset, Antoni Lombarte, and Carlos A Assis. Otolith atlas for the western mediterranean, north and central eastern atlantic. *Scientia Marina*, 72(S1):7–198, 2008.
- [12] Joseph I Goldstein, Dale E Newbury, Joseph R Michael, Nicholas WM Ritchie, John Henry J Scott, and David C Joy. *Scanning electron microscopy and X-ray microanalysis*. Springer, 2017.
- [13] Antoni Lombarte and José M Fortuño. Differences in morphological features of the sacculus of the inner ear of two hakes (*merluccius capensis* and *m. paradoxus*, gadiformes) inhabits from different depth of sea. *Journal of Morphology*, 214(1):97–107, 1992.
- [14] Gabriel J Torres, Antoni Lombarte, and Beatriz Morales-Nin. Variability of the sulcus acusticus in the sagittal otolith of the genus *merluccius* (merlucciidae). *Fisheries Research*, 46(1-3):5–13, 2000.
- [15] Karin Hüsse. Otolith shape in juvenile cod (*gadus morhua*): Ontogenetic and environmental effects. *Journal of Experimental Marine Biology and Ecology*, 364(1):35–41, 2008.
- [16] Matthew D Taylor, Ashley M Fowler, and Iain M Suthers. Insights into fish auditory structure–function relationships from morphological and behavioural ontogeny in a maturing sciaenid. *Marine Biology*, 167(2):1–11, 2020.
- [17] Avinash C Kak, Malcolm Slaney, and Ge Wang. Principles of computerized tomographic imaging. *Medical Physics*, 29(1):107–107, 2002.
- [18] Ashesh B Jani, Charles A Pelizzari, George TY Chen, John Roeske, Russell J Hamilton, R Loch Macdonald, Frank Bova, Kenneth R Hoffmann, and Patrick A Sweeney. Volume rendering quantification algorithm for reconstruction of ct volume-rendered structures. 1. cerebral arteriovenous malformations. *IEEE transactions on medical imaging*, 19(1):12–24, 2000.
- [19] Tanja Schulz-Mirbach, Friedrich Ladich, Martin Plath, and Martin Heß. Enigmatic ear stones: what we know about the functional role and evolution of fish otoliths. *Biological Reviews*, 94(2):457–482, 2019.
- [20] Antoni Lombarte. Changes in otolith area: sensory area ratio with body size and depth. *Environmental Biology of Fishes*, 33(4):405–410, 1992.
- [21] Will J Schroeder, Bill Lorensen, and Ken Martin. *The visualization toolkit: an object-oriented approach to 3D graphics*. Kitware, 2004.

- [22] Gary Bradski and Adrian Kaehler. Opencv. *Dr. Dobb's journal of software tools*, 3, 2000.
- [23] Charles R Harris, K Jarrod Millman, Stéfan J van der Walt, Ralf Gommers, Pauli Virtanen, David Cournapeau, Eric Wieser, Julian Taylor, Sebastian Berg, Nathaniel J Smith, et al. Array programming with numpy. *Nature*, 585(7825):357–362, 2020.
- [24] Philippe Thévenaz, Thierry Blu, and Michael Unser. Image interpolation and resampling. *Handbook of medical imaging, processing and analysis*, 1(1):393–420, 2000.
- [25] Dieter Schmalstieg and Robert F Tobler. Real-time bounding box area computation. *Vienna University of Technology*, 1999.
- [26] Wes McKinney et al. pandas: a foundational python library for data analysis and statistics. *Python for High Performance and Scientific Computing*, 14(9), 2011.
- [27] John D Hunter. Matplotlib: A 2d graphics environment. *Computing in science & engineering*, 9(3):90–95, 2007.
- [28] Fredrik Lundh. An introduction to tkinter. *URL: www. pythonware. com/library/tkinter/introduction/index. htm*, 1999.
- [29] Salem Saleh Al-Amri, NV Kalyankar, and SD Khamitkar. Image segmentation by using edge detection. *International journal on computer science and engineering*, 2(3):804–807, 2010.
- [30] Salem Saleh Al-Amri, Namdeo V Kalyankar, et al. Image segmentation by using threshold techniques. *arXiv preprint arXiv:1005.4020*, 2010.
- [31] Alan P Mangan and Ross T Whitaker. Partitioning 3d surface meshes using watershed segmentation. *IEEE Transactions on Visualization and Computer Graphics*, 5(4):308–321, 1999.
- [32] Pauli Virtanen, Ralf Gommers, Travis E Oliphant, Matt Haberland, Tyler Reddy, David Cournapeau, Evgeni Burovski, Pearu Peterson, Warren Weckesser, Jonathan Bright, et al. Scipy 1.0: fundamental algorithms for scientific computing in python. *Nature methods*, 17(3):261–272, 2020.
- [33] Abraham Savitzky and Marcel JE Golay. Smoothing and differentiation of data by simplified least squares procedures. *Analytical chemistry*, 36(8):1627–1639, 1964.
- [34] Jack E Bresenham. Incremental line compaction. *The Computer Journal*, 25(1):116–120, 1982.

- [35] William E Lorensen and Harvey E Cline. Marching cubes: A high resolution 3d surface construction algorithm. *ACM siggraph computer graphics*, 21(4):163–169, 1987.
- [36] Simon Fuhrmann, Michael Kazhdan, and Michael Goesele. Accurate isosurface interpolation with hermite data. In *2015 International Conference on 3D Vision*, pages 256–263. IEEE, 2015.
- [37] Wilhelm Burger and Mark J Burge. *Digital image processing: an algorithmic introduction using Java*. Springer Science & Business Media, 2009.
- [38] Jerry R Van Aken. An efficient ellipse-drawing algorithm. *IEEE Computer Graphics and Applications*, 4(9):24–35, 1984.
- [39] Francesca Vitale, Lotte Worsøe Clausen, and Gráinne Ní Chonchúir. Handbook of fish age estimation protocols and validation methods, 2019.
- [40] Enrique Macpherson, Beatriz Roel, and Beatriz Morales-Nin. Reclutamiento de la merluza y abundancia y distribucion de diferentes especies comerciales en las divisiones 1.4 y 1.5 durante 1983-1984. 1985.
- [41] Fabian Pedregosa, Gaël Varoquaux, Alexandre Gramfort, Vincent Michel, Bertrand Thirion, Olivier Grisel, Mathieu Blondel, Peter Prettenhofer, Ron Weiss, Vincent Dubourg, et al. Scikit-learn: Machine learning in python. *the Journal of machine Learning research*, 12:2825–2830, 2011.
- [42] Paolo Cignoni, Marco Callieri, Massimiliano Corsini, Matteo Dellepiane, Fabio Ganovelli, and Guido Ranzuglia. Meshlab: an open-source mesh processing tool. In *Eurographics Italian chapter conference*, volume 2008, pages 129–136. Salerno, 2008.
- [43] Erik LG Wernersson, Cris L Luengo Hendriks, and Anders Brun. Accurate estimation of gaussian and mean curvature in volumetric images. In *2011 International Conference on 3D Imaging, Modeling, Processing, Visualization and Transmission*, pages 312–317. IEEE, 2011.
- [44] Timothy D Gatzke and Cindy M Grimm. Estimating curvature on triangular meshes. *International journal of shape modeling*, 12(01):1–28, 2006.
- [45] John R Baumgardner and Paul O Frederickson. Icosahedral discretization of the two-sphere. *SIAM Journal on Numerical Analysis*, 22(6):1107–1115, 1985.
- [46] Michael Garland and Paul S Heckbert. Surface simplification using quadric error metrics. In *Proceedings of the 24th annual conference on Computer graphics and interactive techniques*, pages 209–216, 1997.

- [47] Gabriel Taubin. Curve and surface smoothing without shrinkage. In *Proceedings of IEEE international conference on computer vision*, pages 852–857. IEEE, 1995.
- [48] David A Field. Laplacian smoothing and delaunay triangulations. *Communications in applied numerical methods*, 4(6):709–712, 1988.
- [49] Martin Ester, Hans-Peter Kriegel, Jörg Sander, Xiaowei Xu, et al. A density-based algorithm for discovering clusters in large spatial databases with noise. In *Kdd*, pages 226–231, 1996.